Burgener AV, Bantug GR, Meyer BJ, Higgins R, Ghosh A, Bignucolo O, Ma EH, Loeliger J, Unterstab G, Geigges M, Steiner R, Enamorado M, Ivanek R, Hunziker D, Schmidt A, Müller-Durovic B, Grählert J, Epple R, Dimeloe S, Lötscher J, Sauder U, Ebnöther M, Burger B, Heijnen I, Martínez-Cano S, Cantoni N, Brücker R, Kahlert CR, Sancho D, Jones RG, Navarini A, Recher M, Hess C. SDHA gain-of-function engages inflammatory mitochondrial retrograde signaling via KEAP1-Nrf2. Nat Immunol. 2019 Oct;20(10):1311-1321.

SDHA gain-of-function engages inflammatory retrograde signaling via KEAP1–Nrf2

Anne-Valérie Burgener[1, 21], Glenn R. Bantug[1, 21], Benedikt Meier[2], Rebecca Higgins[3], Adhideb Gosh[3, 4], Olivier Bignucolo[5], Eric H. Ma[6], Jordan Löliger[1], Gunhild Unterstab[1], Marco Geigges[7], Rebekah Steiner[1], Michel Enamorado[8, 9], Robert Ivanek[10], Danielle Hunziker[1], Alexander Schmidt[11], Bojana Müller-Durovic[1], Jasmin Grählert[1], Raja Epple[1], Sarah Dimeloe[12], Jonas Lötscher[1], Ursula Sauder[13], Monika Ebnöther[14], Bettina Burger[3], Ingmar Heijnen[15], Sarai Martínez-Cano[8], Nathan Cantoni[16], Rolf Brücker[17], Christian R. Kahlert[18], David Sancho[8], Russell G. Jones[6, 19], Alexander Navarini[3], Mike Recher[2, 21], Christoph Hess[1, 20, 21, *]

[1] Immunobiology Laboratory, Department of Biomedicine, University and University Hospital of Basel, Basel, Switzerland
[2] Immunodeficiency Laboratory, Department of Biomedicine, University and University Hospital of Basel, Basel, Switzerland
[3] Division of Dermatology and Dermatology Laboratory, Department of Biomedicine, University and University Hospital of Basel, Basel, Switzerland
[4] Competence Center for Personalized Medicine University of Zürich/ETH, Zürich, Switzerland
[5] Department of Pharmacology and Toxicology, University of Lausanne, Lausanne, Switzerland
[6] Goodman Cancer Research Centre; Department of Physiology, McGill University, Montreal, Canada
[7] Epigenomics Group, D-BSSE, ETH Zürich, Basel, Switzerland
[8] Immunobiology Laboratory, Centro Nacional de Investigaciones Cardiovasculares Carlos III (CNIC), Madrid, Spain
[9] Mucosal Immunology Section, Laboratory of Parasitic Diseases, NIAID, NIH, Washington DC, USA
[10] Bioinformatics Facility, Department of Biomedicine, University and University Hospital of Basel, Basel, Switzerland
[11] Proteomics Core Facility, Biozentrum, University of Basel, Basel, Switzerland
[12] Institute of Immunology and Immunotherapy, University of Birmingham, Birmingham, UK
[13] Electron Microscopy Core Facility, Biozentrum, University of Basel, Basel, Switzerland
[14] Division of Hematology and Oncology, Claraspital, Basel, Switzerland
[15] Division Medical Immunology, Laboratory Medicine, University Hospital Basel, Basel, Switzerland
[16] Division of Hematology, Cantonal Hospital of Aarau, Aargau, Switzerland
[17] Division of Internal Medicine and Rheumatology, Hospital St. Anna, Luzern, Switzerland
[18] Division of Infectious Diseases, Children's Hospital of St. Gallen, St. Gallen, Switzerland
[19] Cancer and Immunometabolism, Van Andel Research Institute, Grand Rapids, MI, USA
[20] Department of Medicine, University of Cambridge, Cambridge, UK

[21] Equal contribution

* Correspondence to: Christoph Hess, MD PhD
Immunobiology Laboratory
Department of Biomedicine
University and University Hospital of Basel
20 Hebelstrasse
CH-4031 Basel
Switzerland
Phone: +41(0)61.265.44.75
Email: chess@uhbs.ch

ABSTRACT

Immune cell metabolism and function are intimately interlinked. Whether screening metabolic activity of immune cells has clinical value, or facilitates discovery of molecular pathology, remains unknown. We prospectively screened glycolysis (extracellular acidification rate – ECAR) and mitochondrial respiration (oxygen consumption rate – OCR) in B cells from healthy subjects (n = 15) and patients with primary antibody deficiency (PAD, n = 14). ECAR was similar in both cohorts, whereas OCR was higher in PAD patients. The highest OCR values grouped three unrelated study participants with persistent polyclonal B cell lymphocytosis (PPBL), a condition characterized immunologically by expansion of marginal zone-like B cells. Guided by this metabolic phenotype, exome sequencing identified – in all three PPBL patients – rare germline mutations in the gene coding for succinate dehydrogenase, subunit A (*SDHA*). These mutations resulted in gain-of-function, driving fumarate accumulation and inhibition of KEAP1. Consequent nuclear accumulation of the transcription factor Nrf2 mediated excess production of IL-6, and other inflammatory cytokines, PPBL B cells. In a single patient trial, blocking IL-6 activity *in vivo* prevented systemic inflammation and ameliorated clinical disease.

Overall, our study identified pathological retrograde signaling as a previously unknown cause of primary immune dysregulation. Specifically, gain-of-function of SDHA led to accumulation of fumarate in PPBL B cells, which engaged the KEAP1–Nrf2 system to drive transcription of inflammatory cytokines. Metabolic screening of a clinically justified cell population thus helped uncover a novel molecular disease mechanism and pinpointed new therapeutic targets.

INTRODUCTION

Primary immunodeficiency disorders (PIDs) are rare genetic syndromes arising from defects in the immune system. More than 350 PID entities have been defined to date[1]. The majority of PID patients display antibody deficiency (primary antibody deficiency – PAD), ranging from agammaglobulinemia to immunoglobulin subclass deficiency[2,3]. PADs can develop due to B cell intrinsic defects, yet causes and genetics of PADs are complex and only in a minority of cases pathogenic mutations have been identified (e.g. mutations in the genes encoding for Ig H and L chain, BLINK or CD19)[4-6]. PADs present with a spectrum of clinical problems, ranging from infections to autoinflammation, autoimmunity, lymphoproliferation (lymphadenopathy, splenomegaly, lymphoma) and enteropathy. Susceptibility to infection is reduced by substitution of immunoglobulins. By contrast, non-infectious complications are typically not affected by immunoglobulin replacement therapy and contribute to excess mortality in these patients[7].

Over the last years our understanding of how cellular metabolism governs immune cell function has rapidly increased[8-11]. Specifically, various facets of glycolysis have been demonstrated to impact the function of many immune cell types, including B cells[12-14]. Glutamine metabolism – critically required for effector T cell-, NK cell-, macrophage- and DC function – is also increased in activated B cells[14-17]. Glutaminolysis can importantly contribute to ATP production, and glutamine-derived α-ketoglutarate (α-KG) serves as anaplerotic source of tricarboxylic acid (TCA) cycle metabolites[15,16,18]. The TCA cycle operates tightly integrated with the respiratory chain within mitochondria[19,20]. Fueled by glycolysis, glutaminolysis or β-oxidation, mitochondrial oxidative phosphorylation (OxPhos) produces most of the ATP required for anabolic processes, including cell proliferation or production of effector molecules secreted by immune cells[21-23]. Importantly, several non-bioenergetic features of mitochondria further critically regulate immune cell function. In LPS-stimulated macrophages accumulation of the TCA cycle intermediate succinate promotes transcription of inflammatory genes by driving mitochondrial hyperpolarization and mitochondrial reactive oxygen species (mROS)

dependent HIF-1α stabilization[24]. In $CD4^+$ T cells, production of mROS has been linked to the activation of NFAT and production of IL-2[25], in B cells to reduced expression of CD19 and inhibition of signaling through the B cell receptor (BCR)[26]. In nascent activated memory $CD8^+$ T cells, mitochondrial function and epigenetic remodeling have been shown to be interlinked via pyruvate oxidation and conversion of pyruvate-derived citrate to acetyl-CoA – which is required for histone acetylation[27,28]. Metabolites of the TCA cycle can also directly activate (α-KG), or inhibit (fumarate, succinate) dioxygenases that are involved in histone and DNA demethylation, thus modulating transcriptional activity (= retrograde signaling)[29,30]. Indeed, the ratio of α-KG to fumarate + succinate has been shown to govern epigenetic changes and transcriptional programs in macrophages[31,32]. Protein succination – the fumarate-dependent, non-enzymatic addition of a succinyl group to thiol groups in proteins – provides another emerging link between mitochondrial function, i.e. fumarate production, and the transcriptional activity of cells[33,34]. In macrophages and T cells, pharmacologically increasing fumarate levels have recently been shown to drive succination events[35], and oxidative stress in type 2-diabetes has likewise been described to promote protein succination[36], as has loss of fumarate hydratase (FH) activity in certain types of cancer[35-37]. In each of these scenarios, succination was demonstrated to alter protein- and thus cellular functions.

In this study we explored whether metabolic screening has potential to guide discovery of molecular disease mechanism in patients with PAD. We found that B cell OxPhos served as functional biomarker that helped decipher pathogenic immunometabolic dysregulation in marginal zone-like B cells, which directed a successful clinical intervention.

RESULTS

Oxygen consumption rates are increased in B cells from patients with primary antibody deficiency.

First, to establish normal values for bulk B cell oxygen consumption (oxygen consumption rates – OCR) and glycolysis (extracellular acidification rates – ECAR), we measured both metabolic parameters in B cells from healthy individuals (n = 15) using a metabolic flux analyzer (**Fig. 1a**). Normal values were then compared with those obtained in B cells from patients with PAD (n = 14) (**Fig. 1a**). Patients with a diagnosis of PAD were prospectively included in the study (inclusion criteria: age ≥ 18 years; total immunoglobulin (Ig) G level < 7g/L, or subclass deficiency (defined as IgG_1 < 4.9 g/l, IgG_2 < 1.5 g/l, IgG_3 < 0.2 g/l or IgG_4 < 0.08 g/l); no evidence for secondary antibody deficiency) and metabolic screening experiments were assessed blinded for clinical information. This prospective screening approach identified higher mean respiratory activity (OCR) in B cells from patients as compared to the healthy control population. Glycolysis, by contrast, was similar in patients and controls (**Fig. 1a**). Distribution of age was comparable between patients and controls, and in either cohort no strong age dependence of OCR or ECAR was observed (**Fig. S1a**). Also, no difference in OCR or ECAR was detected between female- and male study participants, and between CMV^+ and CMV^- individuals (**Fig. S1b**). Three patients with a particularly high OCR, which we have labeled hyper-respiration, stood out from this analysis (Patients #1, #8, and #9) (**Tbl. S1a**). Intriguingly, these 3 non-related patients all had the same disease, namely *Persistent Polyclonal B Cell Lymphocytosis* (PPBL). PPBL is a rare disorder, originally described by Gordon *et al.* in 1982 (Ref. [38]), characterized by expansion of B cells with a marginal zone-like phenotype ($CD19^+$ $CD27^+$ IgD^+), evidence of bi-nucleated lymphocytes, elevated levels of serum IgM and – the inclusion criterion for this study – low levels of IgG. The etiology of PPBL is not known, yet cigarette smoking in combination with a genetic basis has been suggested[39,40]. PPBL is often clinically silent or oligosymptomatic, yet it may also present with signs and symptoms of severe immune dysregulation and it can evolve toward clonal proliferation or overt malignant lymphoma[41,42]. The three PPBL patients included in this study all were heavy smokers

and had clinically manifest disease, specifically one or several of the following: recurrent bronchitis (n = 3); hepato- / splenomegaly (n = 3); recurrent sinusitis (n = 2); arthralgia (n = 1); Raynaud syndrome (n = 1); spontaneous rib fracture (n = 1); candida esophagitis (n = 1); recurrent herpes simplex (n = 1); recurrent otitis (n = 1); weight loss (n = 1); fatigue (n = 1); large and small vessel vasculitis (n = 1); scleritis (n = 1); tendinitis (n = 1), and perichondritis (n = 1). Clinical and immunologic characteristics of all PAD study participants, including the 3 PPBL patients, are summarized in **Table S1a** and **S1b**, respectively. From the PPBL patient with the most severe disease course (Patient #9), **Figure 1b** provides a summary of C-reactive protein (CRP – reflecting systemic inflammation) values over time, and associated disease signs and symptoms; a representative histology image demonstrating cutaneous small-vessel vasculitis (leukocytoclastic vasculitis), and a CT scan depicting periaortitis. In **Figure 1c** and **Figure S1c** representative examples of the B cell surface phenotype (expression of IgD, CD27, CD24, CD38 and TACI) in PPBL patients vs. healthy controls is shown. B cells from PPBL patients almost exclusively displayed a marginal zone-like phenotype. Next, we assessed proliferation of $IgD^{+}CD27^{-}$ and $IgD^{+}CD27^{+}$ B cells from healthy donors, as well as PPBL B cells upon stimulation with either CpG or IL-21 and CD40L. Proliferation of healthy control $IgD^{+}CD27^{-}$ and $IgD^{+}CD27^{+}$ and PPBL B cells was comparable (**Figure S1d**). To test whether hyper-respiration was an intrinsic feature of marginal zone-like B cells, we compared the OCR of PPBL B cells with that from sorted marginal zone-like B cells of healthy individuals. The OCR of marginal zone-like B cells from healthy individuals was similar when compared to that of bulk B cells (**Fig. 1d**, upper left panel). Next, temporal stability of hyper-respiration among PPBL B cells was determined by re-assessing the OCR ~12 months after baseline measurements, at times of routine controls. No change in the respiratory phenotype was observed, establishing its robustness over time – and its independence of clinical disease activity (**Fig. 1d**, lower left panel). Hyper-respiration of PPBL B cells was also unaffected by *in vivo* exposure to a rapalogue (sirolimus) (**Fig. 1e**), which was used in Patient #9 in an (unsuccessful) attempt to control large vessel vasculitis. Sirolimus-resistance of the OCR further pointed to a distinct stability of this metabolic phenotype. In contrast to mitochondrial respiration, basal glycolysis was similar in PPBL

patients and healthy controls, and also not different between marginal zone-like- and bulk B cell populations (**Fig. 1d**, upper right panel). Glycolysis, like oxygen consumption, was also stable over time – although being somewhat more variable (**Fig. 1d**, lower right panel). In both, healthy- and PPBL B cells, glycolysis similarly increased when mitochondrial respiration was pharmacologically shut down (data not shown), as well as when B cells were stimulated with IL-21 and CD40L (**Fig. 1f**). Lastly, glucose uptake was not different between healthy- and PPBL B cells (**Fig. 1g**).

Of note, relative distribution of T cell subpopulations and proliferation of $CD4^+$ and $CD8^+$ T cells was similar in healthy controls and PPBL patients (**Fig. S1e**,**f**). Additionally, there was no evidence for altered antigen-specific T cell function against CMV epitopes (**Fig. S1g**). Bulk T cells from PPBL patients did not differ in basal respiration and glycolysis from healthy control T cells, nor was mitochondrial membrane potential altered between groups (**Fig. S1h**). Together these data identified hyper-respiration, at the cohort level, as an immunometabolic trait of primary bulk B cells in patients with PAD. The three study participants with the clinical diagnosis of PPBL demonstrated B cell-intrinsic hyper-respiration, which was confirmed in two additional patients with PPBL, and not found in healthy marginal zone-like (MZ-like) B cell counterparts. Furthermore, no evidence for altered T cell function or metabolism was observed in PPBL patients, alluding to a B cell-specific dysregulation of mitochondrial respiration.

Figure 1

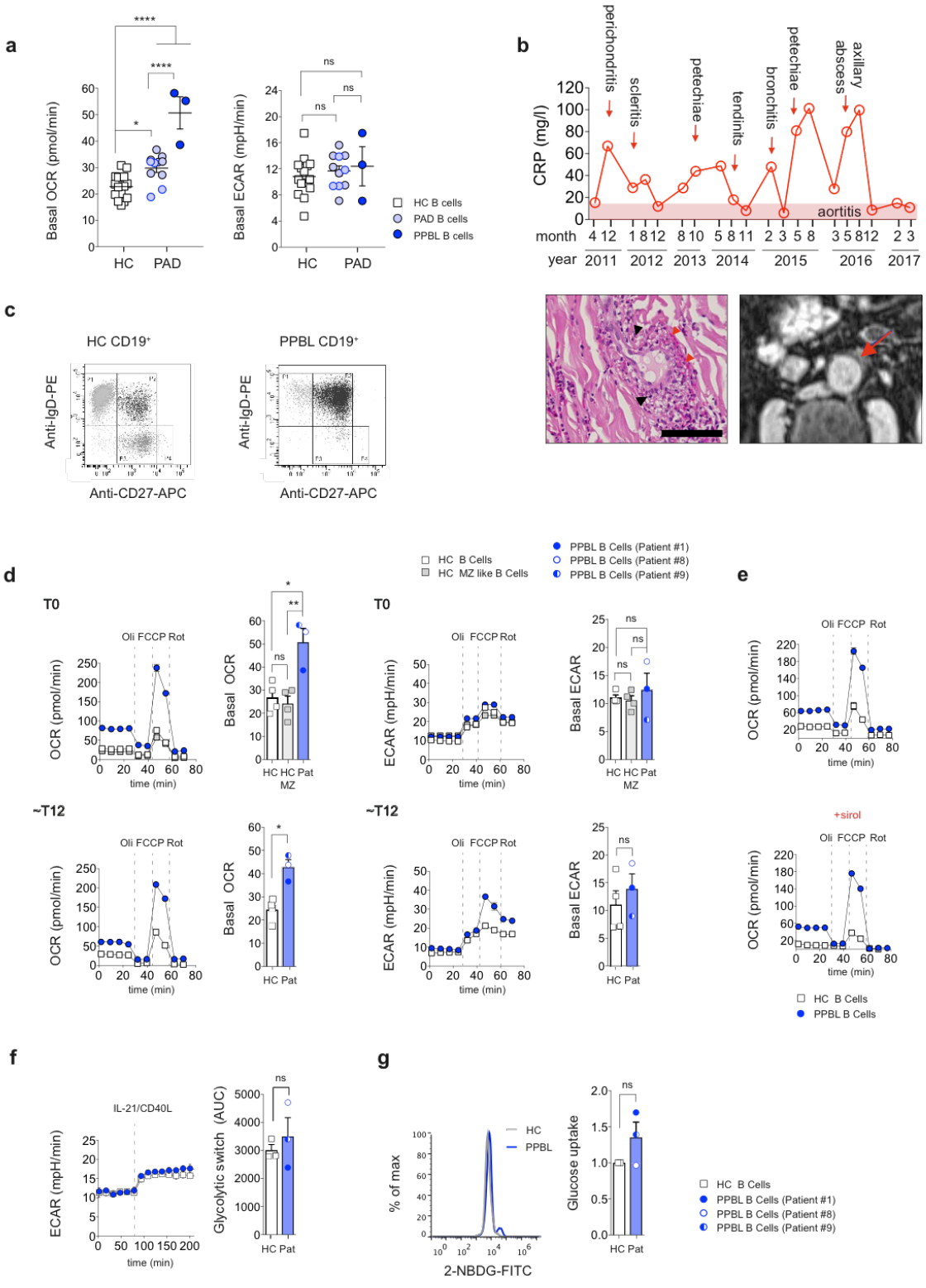
a
Basal OCR (pmol/min)
Basal ECAR (mpH/min)
HC
PAD
HC B cells
PAD B cells
PPBL B cells
b
CRP (mg/l)
perichondritis
sclerits
petechiae
tendinits
bronchitis
petechiae
abscess
axillary
aortitis
month
year
c
HC CD19+
PPBL CD19+
Anti-IgD-PE
Anti-CD27-APC
d
HC B Cells
HC MZ like B Cells
PPBL B Cells (Patient #1)
PPBL B Cells (Patient #8)
PPBL B Cells (Patient #9)
T0
~T12
Oli FCCP Rot
OCR (pmol/min)
ECAR (mpH/min)
time (min)
Basal OCR
Basal ECAR
HC HC Pat MZ
HC Pat
e
+sirol
f
IL-21/CD40L
Glycolytic switch (AUC)
g
% of max
HC
PPBL
2-NBDG-FITC
Glucose uptake

Legend to Figure 1: Metabolic B cell profile of healthy controls and patients with primary antibody deficiency.

(**a**) Basal mitochondrial respiration (oxygen consumption rate – OCR) (*left panel*) and basal glycolysis (extracellular acidification rate – ECAR) (*right panel*) of bulk B cells from healthy controls (HCs) (n = 15) and patients with primary antibody deficiency (PAD) (n = 14). Patients (n = 3) with persistent polyclonal B cell lymphocytosis (PPBL) had the highest OCR values. (**b**) *Upper panel:* C-reactive protein (CRP) measurements over time (red line) and clinical symptoms (red arrows) from Patient #9. *Lower panel:* Left, histopathology of a skin biopsy, depicting leukocytoclastic vasculitis (perivascular neutrophilic infiltration and nuclear debris (black arrowheads), and deposition of fibrin (red arrowheads)). Scale bar, 100 μm. Right, abdominal CT scan showing a contrast enhanced soft-tissue dense area (red arrow) around the aorta, reflecting periaortitis. (**c**) Representative flow cytometry dot plots from a HC and a PPBL patient showing subset distribution of $CD19^+$ B cells stained with IgD and CD27 antibodies. (**d**) Representative baseline OCR and ECAR measurements (T0) of primary B cells or primary MZ-like B cells from HCs, and primary B cells from PPBL patients. Shown are basal values and measurements following mitochondrial perturbation with oligomycin (Oli), FCCP, and rotenone (Rot). Summary bar graphs represent basal respiration (OCR) and basal glycolysis (ECAR) of primary B cells (n = 4), primary MZ-like B cells (n = 4) from HCs, and primary B cells from PPBL patients (n = 3). *Lower panels:* Follow-up one year after baseline assessment (= T12), showing representative OCR and ECAR measurements of primary B cells from a HC and primary B cells from a PPBL patient. Mitochondrial perturbation was performed as above. Summary bar graphs represent T12 basal respiration (OCR) and T12 basal glycolysis (ECAR) of primary B cells from HCs (n = 3), and primary B cells from PPBL patients (n = 3). (**e**) Mitochondrial perturbation profiles of primary B cells from a HC, and from PAD Patient #9 before (*upper panel*) and during sirolimus (2 mg/d) treatment of the patient (*lower panel* – treatment duration at the time of analysis: 2.5 months). (**f**) Representative ECAR measurements of primary B cells from a HC and a PPBL patient before and following injection of IL-21 plus CD40L directly into the metabolic flux analyzer (dashed line). The bar graph summarizes glycolytic switching, calculated as area under the curve (AUC) after activation of primary B cells from HCs (n = 3) and PPBL patients (n = 3). (**g**) Representative flow cytometry histogram, reflecting glucose (2-NBDG) uptake of activated primary B cells from a HC and a PPBL patient. The bar graph summarizes glucose uptake calculated as geometric mean fluorescence (gMFI) of activated primary B cells from PPBL patients (n = 3) relative to that of HCs (n = 3). Cells were activated with IL-21 plus CD40L for 24 hours prior to analysis.

Data are represented as mean ± SEM. Statistical significance was assessed by one-way ANOVA (**a**), or unpaired t-test (**d**-**g**). * $p < 0.05$, ** $p < 0.01$, *** $p < 0.001$, **** $p < 0.0001$, ns, not significant. See also **Figure S1**.

Mitochondrial morphology and expression of respiratory chain proteins is normal in PPBL B cells.

Given the robustness of the hyper-respiratory B cell phenotype among PPBL patients, we went on to analyze mitochondrial content and ultrastructure of primary PPBL B cells in comparison to primary bulk B cells from healthy donors. No differences in cristae and matrix morphology were identified. Mitochondrial number and area per cell, as well as the total cell area, was similar between B cells from PPBL patients and healthy donors (**Fig. S2a**). Mitochondrial shape (aspect ratio = length/width) in B cells from PPBL patients was also similar to that of healthy donors (**Fig. S2a**). We then probed for protein abundance of components from each of the respiratory chain complexes, specifically NDUFB8 (complex I); succinate dehydrogenase (SDH) B (complex II); UQCRC2 (complex III); COX II (complex IV), and ATP5A (complex V) from representative healthy control and PPBL patient primary B cells. None of these proteins differed in abundance between primary PPBL B cells and healthy donor B cells (**Fig. S2b**). To further define whether abundance of respiratory chain complexes or super-complex formation differed between normal and PPBL B cells, blue native (BN)-PAGE immunoblot analyses was used. Due to limited availability of primary patient material, mitochondria enriched from EBV-immortalized B cell lines (B-LCLs) were analyzed. In both, cell lines from healthy marginal zone-like B cells and PPBL B cells, expression levels of complexes I–IV were similar. Also formation of complex I containing super-complexes (I + III and I + III + IV), and assembly of complex III + IV, was similar between both groups (**Fig. S2c**). Lastly, we also stained primary B cells from healthy donors and from PPBL patients with mitochondrial membrane potential dependent dyes, MTR and MTDR. While mitochondrial abundance and morphology were similar (**Fig. S2a**), staining with both dyes was moderately increased in PPBL B cells (**Fig. S2d**). Lastly, mROS levels were also similar between both cell lines (data not shown). Increased mitochondrial membrane potential thus was the sole difference captured in these experiments, indicative of a subtle, yet robust (see **Fig. 1d**), difference in mitochondrial *function* that is possibly driving the increased OCR of PPBL B cells.

Complex II is hyper-functional in PPBL B cells.

With no evidence for (i) differential mitochondrial abundance, (ii) altered mitochondrial morphology, or (iii) differences in expression levels- or interaction of respiratory chain proteins, we next probed the function of each of the complexes individually. To that end, enzyme activity assays and metabolic flux studies were used to compare the respective mitochondrial functions in cell lines from healthy marginal zone-like B cells and PPBL B cells. Testing enzyme activities individually, activities of complexes I, IV and V were identical in both cell populations. Activity of complex II was, however, robustly increased in all PPBL B cell lines (**Fig. 2a**), providing strong evidence for a specific mitochondria-intrinsic (i.e. complex II-intrinsic) gain-of-function in these cells. To test the function of the respiratory complexes (I–IV) in their normal structural context, their contribution to oxygen consumption was assessed in permeabilized cells[43]. Also in these metabolic flux-based studies a selective increase in the function of complex II was observed (**Fig. 2b**). To ensure that increased complex II-mediated respiration was not fueled through augmented activity of complex I, rotenone, a complex I inhibitor, was used. Blocking complex I did not alter the difference of complex II-driven respiration between B cell lines from healthy donors and PPBL patients (**Fig. 2c**). With these functional data in mind, additional immunoblot analyses were performed, focusing on a subunit of complex I involved in electron transfer (Grim19) and the major catalytic subunit of complex II (SDHA). These experiments again did not detect differential protein abundance between patients and controls – further pointing to enhanced complex II function independent of protein quantity (**Fig. 2d**)[44,45]. These experiments were compatible with the hypothesis that an SDH/complex II gain-of-function phenotype could drive the increased OCR detected in the B cell screening assays of the PPBL study participants.

Figure 2

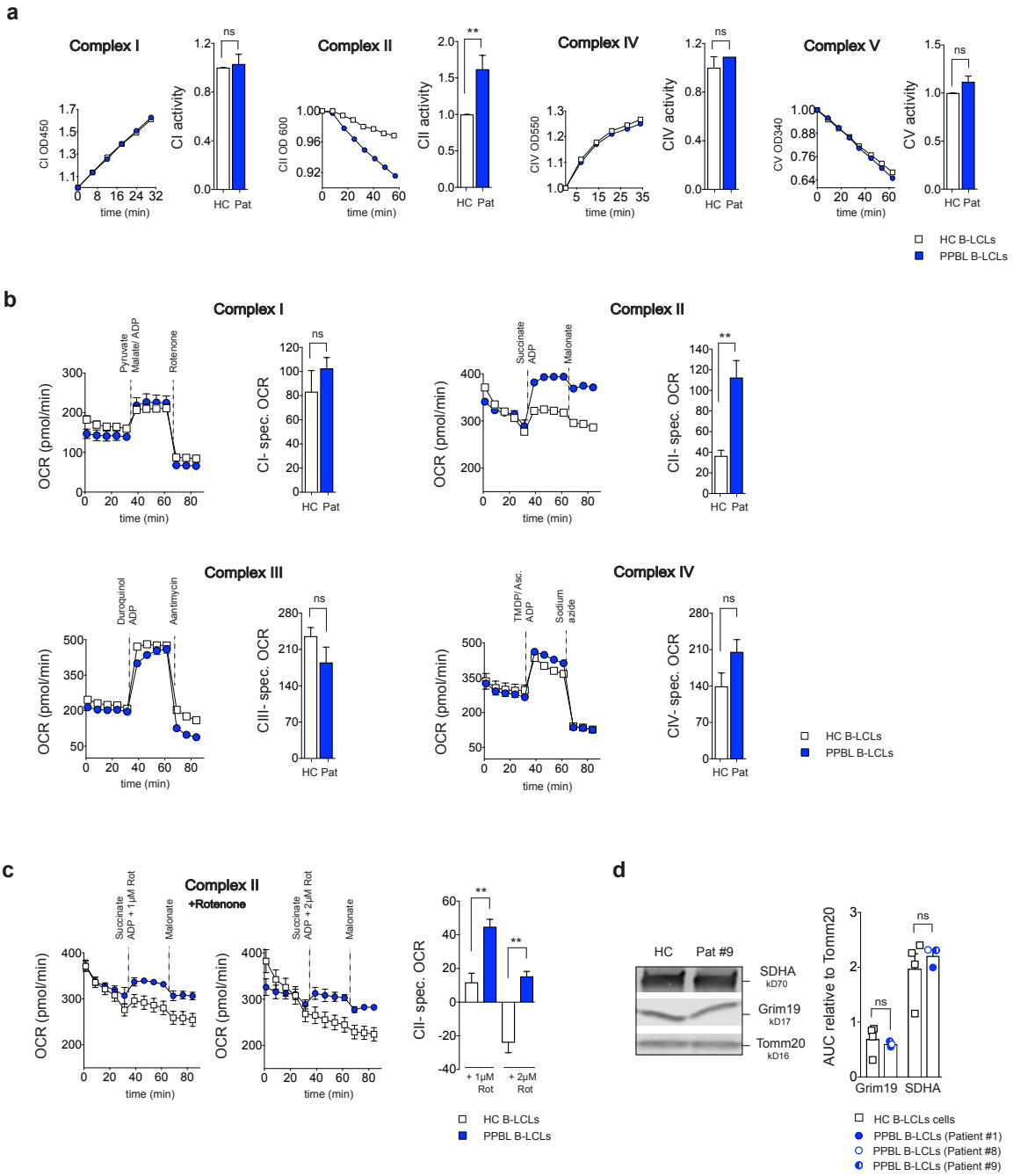
a
Complex I
CI OD450
time (min)
CI activity
HC Pat
ns
Complex II
CII OD 600
time (min)
CII activity
**
Complex IV
CIV OD550
time (min)
CIV activity
Complex V
CV OD340
time (min)
CV activity
HC B-LCLs
PPBL B-LCLs
b
Complex I
Pyruvate
Malate/ ADP
Rotenone
OCR (pmol/min)
time (min)
CI- spec. OCR
Complex II
Succinate
ADP
Malonate
CII- spec. OCR
Complex III
Duroquinol
ADP
Aantimycin
CIII- spec. OCR
Complex IV
TMDP/Asc.
ADP
Sodium
azide
CIV- spec. OCR
c
Complex II
+Rotenone
Succinate
ADP + 1µM Rot
Malonate
Succinate
ADP + 2µM Rot
CII- spec. OCR
+ 1µM Rot
+ 2µM Rot
d
HC
Pat #9
SDHA
kD70
Grim19
kD17
Tomm20
kD16
AUC relative to Tomm20
Grim19
SDHA
HC B-LCLs cells
PPBL B-LCLs (Patient #1)
PPBL B-LCLs (Patient #8)
PPBL B-LCLs (Patient #9)

Legend to Figure 2: Activity of individual mitochondrial respiratory chain complexes in PPBL B cells.

(**a**) Representative activity-assays for CI, CII, CIV, and CV, depicted as changes in absorbance over time, comparing B-LCLs from HCs and PPBL patients. Summary graphs represent activity-rates of individual complexes from PPBL patients (n = 3) relative to those of HCs (n = 3-4). (**b**) Representative OCR measurements of permeabilized B-LCLs from a HC and a PPBL patient prior to and following addition of complex specific substrates and inhibitors, as indicated (dashed lines). Summary graphs represent changes in complex-specific OCR of permeabilized B-LCLs from HCs (n = 3-4) and PPBL patients (n = 3). (**c**) Representative OCR measurements of permeabilized B-LCLs of a HC and a PPBL patient, prior to and following addition of succinate, ADP and rotenone or inhibitors, as indicated (dashed lines). The bar graph summarizes changes in complex II-specific OCR of permeabilized B-LCLs from HCs (n = 3) and PPBL patients (n = 3), following addition of CII substrate (succinate, ADP) and subsequent inhibition of CI with rotenone. (**d**) Representative immunoblot analysis of isolated mitochondria from B-LCLs of a HC and one PPBL patient. Blots were probed for Complex I subunit Grim19, Complex II subunit SDHA, and Tomm20. The bar graph summarizes the abundance of Grim19 and SDHA, normalized to Tomm20, in isolated mitochondria of B-LCLs derived from HCs (n = 4) and PPBL patients (n = 3).

Pooled data are represented as mean ± SEM. Statistical significance was assessed by unpaired t-test (**a**-**d**). * $p < 0.05$, ** $p < 0.01$, ns, not significant. See also **Figure S2**.

Glutaminolysis contributes to TCA fueling in SDH hyper-functional PPBL B cells.

To gain insight into the metabolic landscape of B cells characterized by this newly identified SDHA gain-of-function phenotype, we performed unbiased metabolomic analyses, comparing primary PPBL B cells with primary sorted marginal zone-like B cells from healthy individuals. The key finding of these experiments was a strong and highly significant accumulation of fumarate, i.e. the direct product of SDH. Not surprisingly, malate, the next metabolite downstream in the TCA cycle (= product of FH)[46], was also more abundant (**Fig. 3a**). With the noticeable exception of succinate, all other TCA cycle metabolites captured in this assay were – albeit to a lesser extent than fumarate and malate – also more abundant in PPBL B cells than in healthy marginal zone-like B cells (**Fig. 3a**). Accumulation of fumarate, the metabolic hallmark of primary PPBL B cells, was maintained in EBV-immortalized B cell lines derived from PPBL B cells (**Fig. 3b**). This metabolite profile was consistent with the increased functional activity of SDH identified in the previous experiments (**Fig. 2a-c**). Since glutamate and α-KG were also significantly more abundant in PPBL B cells, the metabolomic data suggested increased glutaminolysis in PPBL B cells as compared to healthy marginal zone-like B cells (**Fig. 3a**). Several glycolytic intermediates were also increased in PPBL B cells (dihydroxyacetone phosphate, 2-phosphoglycerate and phosphoenolpyruvate), whereas pyruvate was similarly abundant. Since ECAR values and glucose uptake were alike in PPBL B cells and healthy marginal zone-like B cells (**Fig. 1a**,**d**,**f** and **Fig. 1g**, respectively) this suggested a buildup of glycolytic intermediates, rather than increased glycolytic flux in PPBL B cells. Of note, whereas the ratio of fumarate over succinate was increased in PPBL B cells, the ratio of α-KG to fumarate + succinate was similar between PPBL B cells and healthy marginal zone-like B cells, since α-KG was also more abundant in these cells (**Fig. 3c**). To directly assess incorporation of glucose- and glutamine-derived carbons in TCA cycle metabolites, metabolic tracing studies were performed on primary PPBL B cells, using uniformly labeled ^{13}C-glucose and ^{13}C-glutamine, respectively (**Fig. 3d**). In these experiments, abundant m+5 (α-KG) and m+4 (succinate, fumarate, malate, and citrate) isotopologues of TCA cycle metabolites were detected in cells cultured

with ^{13}C-glutamine, confirming that glutaminolysis contributed to anaplerotic fueling of the TCA cycle in PPBL B cells. In addition, the presence of m+2 isotopologues of α-KG, succinate, fumarate and malate from glutamine-derived carbons suggested more than one round of metabolism through the TCA cycle. Combined these metabolomic and tracing studies (i) confirmed accumulation of fumarate – in line with SDH overshoot function (**Fig. 2a-c**), and (ii) suggested glutamine as an important fuel source of the TCA cycle in PPBL B cells.

Figure 3

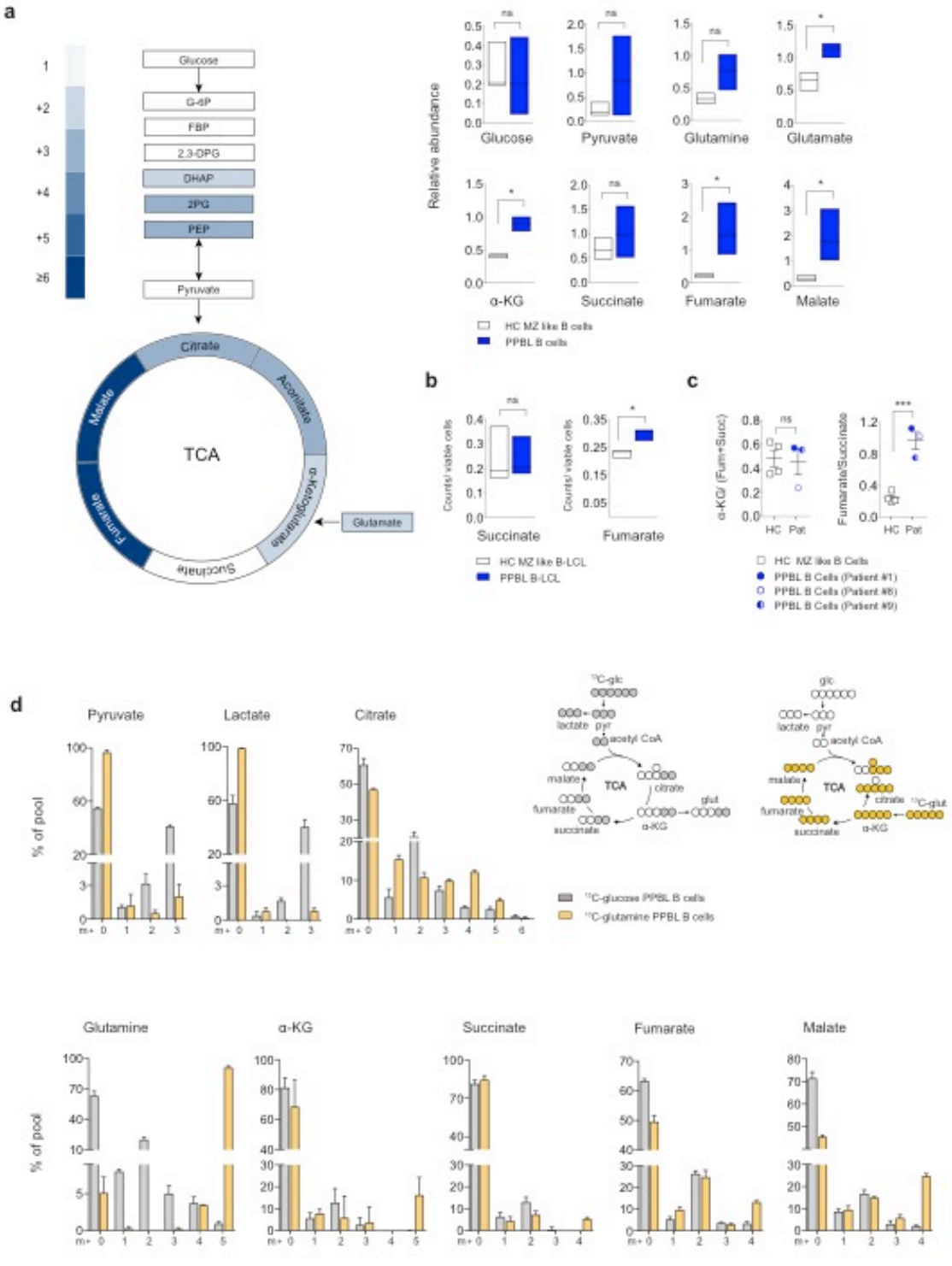
a
1
+2
+3
+4
+5
≥6
Glucose
G-6P
FBP
2,3-DPG
DHAP
2PG
PEP
Pyruvate
Citrate
Aconitate
α-Ketoglutarate
Succinate
Fumarate
Malate
TCA
Glutamate
Relative abundance
Glucose
Pyruvate
Glutamine
Glutamate
α-KG
Succinate
Fumarate
Malate
HC MZ like B cells
PPBL B cells
b
Counts/ viable cells
Succinate
Fumarate
HC MZ like B-LCL
PPBL B-LCL
c
α-KG/ (Fum+Succ)
Fumarate/Succinate
HC
Pat
HC MZ like B Cells
PPBL B Cells (Patient #1)
PPBL B Cells (Patient #8)
PPBL B Cells (Patient #9)
d
Pyruvate
Lactate
Citrate
% of pool
m+
13C-glc
lactate
pyr
acetyl CoA
malate
TCA
citrate
glut
fumarate
succinate
α-KG
13C-glut
13C-glucose PPBL B cells
13C-glutamine PPBL B cells
Glutamine
α-KG
Succinate
Fumarate
Malate

Legend to Figure 3: Metabolic characterization of PPBL B cells.

(**a**) *Left panel:* Fold change differences of glycolysis and TCA cycle metabolites between primary B cells from PPBL patients (n = 3) and primary MZ-like B cells from HCs (4 samples pooled of n = 7 donors). Significantly different metabolites are shown in color, with the fold change color-coded from light to dark blue. *Right panels:* Relative abundance of glycolysis and TCA cycle metabolites in primary MZ-like B cells from HCs and primary B cells from PPBL patients (donors as in left panel). (**b**) Abundance of succinate and fumarate in EBV immortalized cells derived from MZ-like B cells from HCs (n = 3) and B cells from PPBL patients (n = 3). (**c**) Ratio of the abundance of α-ketoglutarate (α-KG) over (succinate + fumarate), and fumarate over succinate, both in primary MZ-like B cells from HCs and primary B cells from PPBL patients (donors as in (a)). (**d**) Metabolic tracing analysis of primary B cells from PPBL patients (n = 3) incubated for 6 hours with ^{13}C-glucose or ^{13}C-glutamine. Bar graphs show distribution of mass isotopomers, the scheme depicts the primary labeling of glucose- and glutamine-derived ^{13}C fuelling into the TCA cycle.

Pooled data are shown as mean ± SEM. Statistical significance was assessed by Welch's two-sample t-test (**a**), unpaired t-test (b,**c**). * $p < 0.05$, *** $p < 0.001$, ns, not significant.

PPBL B cells have an inflammatory transcriptional profile.

Having characterized the metabolic alteration and fuel usage of PPBL B cells, we further investigated the transcriptional profile of primary PPBL B cells in comparison to their metabolically non-affected counterpart, i.e. marginal zone-like B cells from healthy blood donors. Of the 13'107 gene transcripts that were detected, mRNA abundance of 1'878 genes (14.33%) differed in a statistically significant manner between the cell types. Unsupervised hierarchical clustering of the samples revealed two groups, corresponding to PPBL B cells and healthy marginal zone-like B cells (**Fig. 4a**, left panel). Globally, only relatively few genes were highly differentially expressed (**Fig. 4a**, right panel). A number of genes typically expressed in marginal zone-like B cells was also abundant in PPBL B cells[47,48], suggesting their close relationship (**Fig. 4b**). Expression of metabolic genes, specifically those involved in the TCA cycle, in glycolysis and in glutamine metabolism, was different between primary patient B cells and healthy marginal zone-like B cells, the fold expression differences were, however, mostly moderate (**Fig. S3a**). Of note, transcripts of mitochondrial complex II genes were not differentially expressed (**Fig. 4c**). mRNA abundance of genes encoding for proteins of the other respiratory complexes was different between the two groups, yet again, fold expression differences were small (**Fig. S3b**).

Importantly, gene products annotated to (i) the inflammatory response and (ii) the IL-6–Jak–Stat3 pathway were enriched in the PPBL samples (**Fig. 4d**). Indeed, transcripts for IL-8, IL-1β, CCL5, IL-6 and TNF were all consistently more abundant in B cells from PPBL patients than marginal zone-like B cells from healthy donors (**Fig. 4e**). Inflammatory cytokines have been described to be produced by marginal zone-like B cells, reflecting their function as innate-like sensors of danger and regulators of the early immune response[47,49,50]. From a clinical perspective, PPBL manifestations pointed to the relevance of IL-6 (a trigger of CRP production by hepatocytes) and IL-8 (a key neutrophil chemoattractant, able to induce acute sterile inflammation such as polychondritis and small vessel vasculitis) (**Fig. 1b**, **Tbl. S1a**)[51,52]. Indeed, IL-6 and IL-8 protein abundance were increased in the

supernatant of B cell lines from PPBL patients compared to marginal zone-like B cell lines from healthy blood donors (**Fig. 4f**). Lastly, the concentration of IL-6, *in vivo*, was moderately increased in 2 of 2 separate measurements from a PPBL patient for which serum samples were available (**Fig. 4g**).

Figure 4

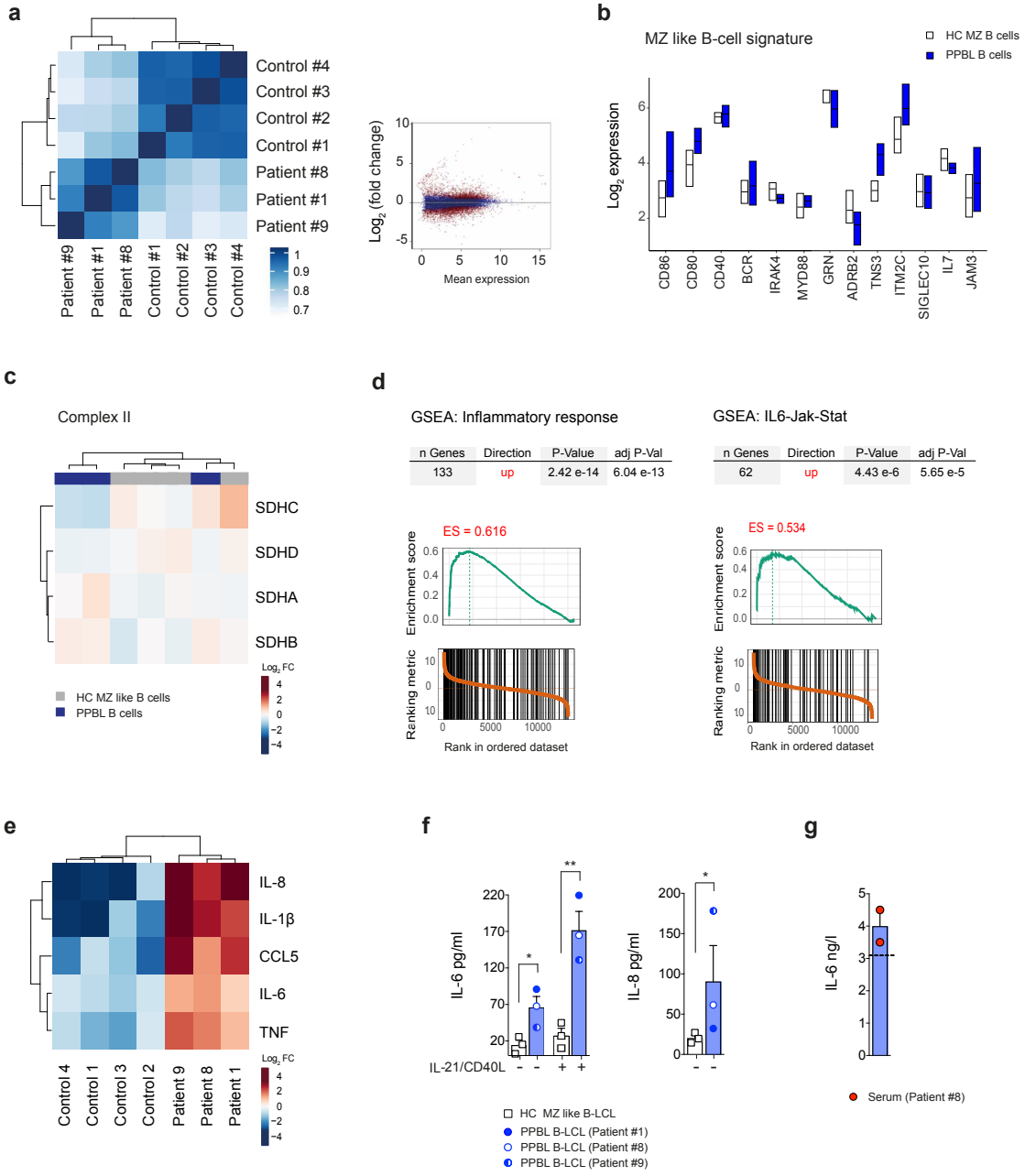
a
Control #4
Control #3
Control #2
Control #1
Patient #8
Patient #1
Patient #9
Patient #9
Patient #1
Patient #8
Control #1
Control #2
Control #3
Control #4
1
0.9
0.8
0.7
Log2 (fold change)
Mean expression
b
MZ like B-cell signature
HC MZ B cells
PPBL B cells
Log2 expression
CD86
CD80
CD40
BCR
IRAK4
MYD88
GRN
ADRB2
TNS3
ITM2C
SIGLEC10
IL7
JAM3
c
Complex II
SDHC
SDHD
SDHA
SDHB
HC MZ like B cells
PPBL B cells
Log2 FC
d
GSEA: Inflammatory response
n Genes
Direction
P-Value
adj P-Val
133
up
2.42 e-14
6.04 e-13
ES = 0.616
Enrichment score
Ranking metric
Rank in ordered dataset
GSEA: IL6-Jak-Stat
n Genes
Direction
P-Value
adj P-Val
62
up
4.43 e-6
5.65 e-5
ES = 0.534
Enrichment score
Ranking metric
Rank in ordered dataset
e
IL-8
IL-1β
CCL5
IL-6
TNF
Control 4
Control 1
Control 3
Control 2
Patient 9
Patient 8
Patient 1
Log2 FC
f
IL-6 pg/ml
IL-8 pg/ml
IL-21/CD40L
HC MZ like B-LCL
PPBL B-LCL (Patient #1)
PPBL B-LCL (Patient #8)
PPBL B-LCL (Patient #9)
g
IL-6 ng/l
Serum (Patient #8)

Legend to Figure 4: Transcriptional profile of PPBL B cells.

(**a**) Hierarchical clustering (heatmap) of sample correlation (*left panel*), and MA plot of transcriptome data (*right panel*) from primary MZ-like B cells of HCs (n = 4) and primary B cells from PPBL patients (n = 3). (**b**) mRNA abundance of MZ-like B cell marker-genes in primary MZ-like B cells from HCs and primary B cells form PPBL patients (donors as in (a)). (**c**) Heatmap of relative expression of genes encoding complex II in primary MZ-like B cells from HCs and primary B cells form PPBL patients (donors as in (a)). (**d**) Gene set enrichment analysis (GSEA) of inflammatory-response genes (*left panel*) and IL-6-Jak-Stat3 pathway genes (*right panel*), transcribed in primary B cells from PPBL patients, compared to MZ-like B cells from HCs (donors as in (a)). ES = enrichment score. (**e**) Heatmap of relative expression of mRNA encoding for IL-8, IL-1β, CCL5, IL-6 and TNF in primary MZ-like B cells from HCs and primary B cells form PPBL patients (donors as in (a)) (**f**) Production of IL-6 and IL-8 protein by MZ-like B-LCLs from HCs (n = 3) and B-LCLs from PPBL patients (n = 3). IL-6 was quantified in culture supernatants of non-activated cells, or cells activated with IL-21 plus CD40L for 48 hours, IL-8 was quantified in supernatants of non-activated cells cultured for 48 hours. Experiments were performed 3-4 times. (**g**) IL-6 protein was quantified in the serum of a PPBL patient. Measurements were performed on two separate occasions (several months apart) when the patient was showing signs and symptoms of active disease and no clinical evidence for infection.

Pooled data are shown as mean ± SEM. Statistical significance was assessed by unpaired t-test (**f**). * $p < 0.05$, ** $p < 0.01$. See also **Figure S3**.

SDH hyper-function drives an inflammatory PPBL B cell phenotype.

Given the inflammatory transcriptome and cytokine output of PPBL B cells, we aimed to assess whether hyperactive SDH and increased cytokine production were linked. First, we probed the effect of the SDH inhibitor 3-nitropropionic acid (3-NPA) on mitochondrial respiration and IL-6 production. Increased OCR of PPBL B cell lines was efficiently reduced by inhibiting SDH with 3-NPA, both in intact cells (**Fig. 5a**, left panel) and in mitochondria of permeabilized cells provided with succinate and ADP (**Fig. 5a**, middle panel). Importantly, basal secretion as well as IL-21 plus CD40L driven production of IL-6 was diminished in PPBL B cell lines in the presence of 3-NPA (**Fig. 5a**, right panel). NPA, at the concentration used, did not affect cell viability (data not shown). A genetic SDHA knockdown system was then utilized to specifically define the impact of SDH activity on production of IL-6. *SDHA*-targeting siRNA reduced SDHA protein expression-levels by approximately 40% (**Fig. 5b**, left panel), which was sufficient to reduce OCR of PPBL B cell lines by around 50% (**Fig. 5b**, middle panel). Reduced SDH (complex II) activity was consistently linked with diminished IL-6 production in PPBL B cell lines from all three patients (**Fig. 5b**, right panel). These experiments clearly established that SDHA activity in PPBL B cells was associated with increased IL-6 output. The data, however, did not clarify whether the product of SDH *per se*, i.e. fumarate, was linked to the inflammatory output of marginal zone-like/PPBL B cells. To address this issue the following experimental strategies were pursued. First, fumarate (in the form of monomethyl fumarate) was added to *in vitro* activated marginal zone-like B cell lines derived from healthy blood donors. Indeed, addition of exogenous fumarate robustly enhanced production of IL-6 in this setting (**Fig. S4a**). Monomethyl fumarate, however, is more electrophilic than fumarate, introducing the potential for unwanted reactivity. Therefore, we induced the buildup of endogenous fumarate by knocking down total FH in B cell lines from healthy marginal zone-like B cells. Indeed, increased abundance of endogenous fumarate in marginal zone-like B cell lines following total FH knockdown increased IL-6 production (**Fig. 5c**). Together these experiments established excess fumarate as an inflammatory trigger that is sufficient in boosting IL-6 production in marginal zone-like B cells. Intriguingly, neither modulation of pyruvate

import nor inhibition of glutaminolysis had a major impact on the capacity of PPBL B cells to produce IL-6, pointing to the intrinsic metabolic flexibility of these cells in fueling SDH activity (**Fig. S4b**).

To gain insight into a possible genetic basis for the SDHA-driven hyper-respiration phenotype observed in the PPBL study participants, whole exome sequencing (WES) of primary B cells was performed. The WES data were first interrogated for all known PID mutations. These analyses did not identify known plausible genetic abnormalities previously linked to a PID (data not shown). We then focused our investigations on rare genetic variants in genes encoding for mitochondrial proteins. This exploration revealed rare variants with a high CADD score in the *SDHA* gene of all three PPBL patients (**Tbl. S2**). The same mutations were also identified in DNA obtained by buccal swabs (data not shown), suggesting germline origin. Since T cells (which also harbored the mutations – data not shown) did not show metabolic alterations, a highly cell-type specific penetrance of the phenotype was established – as is true for most, if not all, germline genetic diseases[53,54]. The family history of all three PPBL patients was not striking, as there was no confirmed or possible PPBL diagnosis in parents or other family members. However, several close relatives were found to suffer from autoimmune thyroid disease and non-specified rheumatic disease, indicative of some level of immune dysregulation.

Aiming to independently confirm these genetic findings, an additional patient with PPBL was recruited into the study. Clinical characteristics of this patient are summarized in **Table S1a**. Hyper-respiration – as a metabolic trait of B cells from PPBL patients – was reproduced also in this study participant (**Fig. S4c**). We then performed WES, which identified a rare genetic variant in the *SDHA* gene also in this patient (**Tbl. S2**), whereas no rare variants in known PID genes were detected.

To experimentally establish, in proof-of-concept, the genotype–phenotype (i.e. gain-of-function) relation for one of the patient mutations, we site-specifically introduced A45T into one allele of marginal zone-like B cell lines from a healthy donor using CRISPR/Cas9 technology. We were able to introduce the site-specific mutation in three independent experiments, and expression of mutated mRNA was confirmed on each occasion (data not shown). In each of these three experiments, introducing A45T was sufficient to augment complex II-specific respiration and IL-6 production (**Fig.**

5d). These proof-of-concept findings established the occurrence of a gain-of-function SDHA mutation that promoted a cell inflammatory response.

We then aimed to obtain structural insight into how this mutation might augment enzyme function at the protein level. SDHA catalyzes oxidation of succinate to fumarate and transfers the resulting electrons to SDHB, which is followed by electron transport to the ubiquinone pool at SDHC-SDHD (succinate quinone reductase)[55]. The SDHA-SDHB complex retains succinate dehydrogenase activity also when dissociated from the membrane-anchoring subunits SDHC and SDHD[56]. We therefore focused our proof-of-concept molecular dynamics (MD) simulations on SDHA and SDHB. Since the side-chain of Thr is highly hydrophilic, as opposed to Ala, we postulated that Thr at position 45 forms hydrogen bonds with SDHB, which may stabilize the complex and favor electron transfer from flavin adenine dinucleotide (FAD) in SDHA to the iron-sulphur clusters in SDHB. H-bonds between the highly flexible SDHA N-terminal segment and SDHB formed randomly and, consequently, at the same rate in both wild type (wt) and A45T mutated SDHA – with approximately 15-20 such events in each of the ~600 nanosecond long trajectories that we analyzed (**Fig. S4d**, and supplementary Video **SV1**). However, while in the scenario with the wt sequence these interactions lasted 2-3 ns and involved mostly one atom pair, they lasted 10-12 ns and involved 2-3 atom-pairs in the case of the A45T mutation (**Fig. 5e, Fig. S4d**, and Video **SV1**). Together this resulted in a stronger hydrogen bond interaction between SDHA and SDHB in presence of the A45T mutation, reflected by an increase in the area under the curve of the hydrogen bonds between the two subdomains (**Fig. 5e**). Residues 43-46 of the N-terminus of SDHA form hydrogen bonds with the SDHB loop connecting β1 and β2. Not surprisingly, this loop in SDHB contains a highly conserved turn formed by Asp20-Pro21-Asp22. Indeed, the two residues Asp20 and Asp22 accounted for more than 90% of the interactions with the SDHA N-terminal segment (**Fig. S4e**). Such a prototypic interaction, in which Ala1, Ser2 and Lys4 of SDHA form hydrogen bonds with Asp20 and Asp22 of SDHB, is shown in **Figure 5f**. Inconsistent with our hypothesis, Thr at the position 45 contributed minimally to the inter-domain contacts. By contrast, as compared to wt, stronger intra-molecular interactions between Thr45 and residues on the adjacent

surface of SDHA were observed. These interactions – involving Arg458, Phe459, Asp511, Arg512, and Met514 – maintained the N-terminal segment in a position along the surface of SDHA, which favors the interaction with SDHB (**Fig. S4f**). Experimentally, stable interactions between SDHA and SDHB were shown to be required for the proper catalytic function of SDHA, both in bacteria and humans[57]. Informed by our MD simulation data, and with this literature in mind, we aimed to experimentally assess the impact of the A45T mutation on compound SDHA-SDHB activity, *in vitro*. Expression of mutant mRNA was confirmed in B cell lines derived from the patient harboring this mutation (**Fig. S4g**, left panel), and compound SDHA-SDHB activity was measured spectrophotometrically in B cell lines from Patient #8, and from healthy controls. In line with the MD simulation model, compound SDHA-SDHB activity was higher in B cell lines from the patient with the A45T mutation, as compared to that in healthy control B cell lines (**Fig. S4g**, right panel). Thus, aligning with the SDHA activity experiments (**Fig. 5d**), the MD data provided structural insight into how A45T may drive the excess function of SDH, namely by increasing interaction between SDHA and SDHB.

Figure 5

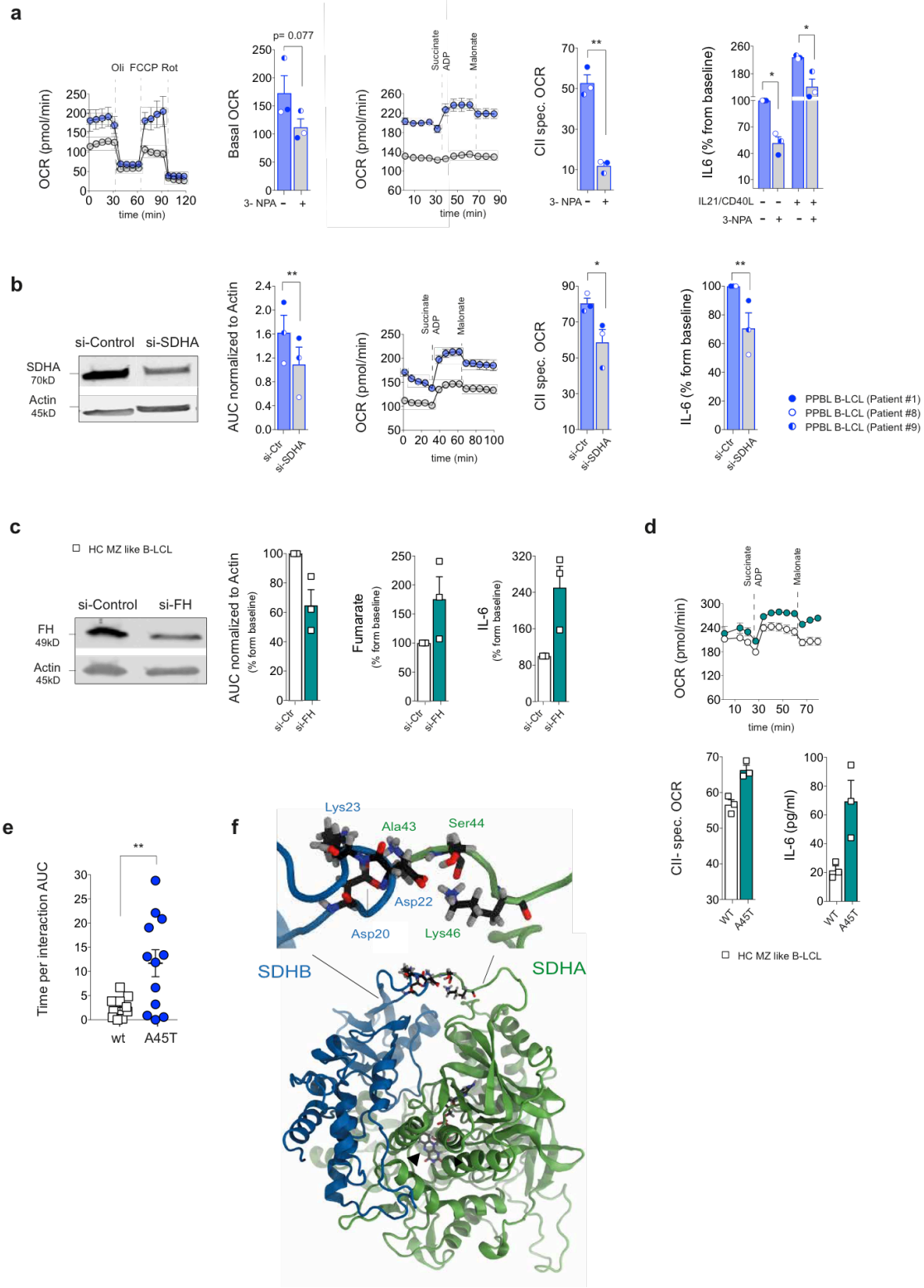
a
Oli FCCP Rot
OCR (pmol/min)
time (min)
Basal OCR
p= 0.077
3- NPA
Succinate
ADP
Malonate
CII spec. OCR
IL6 (% from baseline)
IL21/CD40L
3-NPA
b
si-Control si-SDHA
SDHA
70kD
Actin
45kD
AUC normalized to Actin
si-Ctr
si-SDHA
PPBL B-LCL (Patient #1)
PPBL B-LCL (Patient #8)
PPBL B-LCL (Patient #9)
IL-6 (% form baseline)
c
HC MZ like B-LCL
si-Control si-FH
FH
49kD
Actin
45kD
AUC normalized to Actin (% form baseline)
Fumarate (% form baseline)
IL-6 (% form baseline)
si-FH
d
OCR (pmol/min)
CII- spec. OCR
IL-6 (pg/ml)
WT
A45T
e
Time per interaction AUC
wt
A45T
f
Lys23
Ala43
Ser44
Asp22
Asp20
Lys46
SDHB
SDHA

Legend to Figure 5: SDHA activity and inflammatory cytokine production.

(**a**) *Left panel:* Representative mitochondrial perturbation profile of B-LCLs from a PPBL patient incubated with the SDHA inhibitor 3-nitropropionic acid (3-NPA), or left untreated, for 12 hours prior to the experiment. The bar graph summarizes basal mitochondrial respiration of B-LCLs from PPBL patients (n = 3) either exposed, or not exposed, to 3-NPA. *Middle panel:* Representative mitochondrial respiration profile of permeabilized B-LCLs from a PPBL patient prior to and following addition of complex II specific substrates (succinate, ADP) and the SDHA inhibitor, malonate, as indicated (dashed lines). B-LCLs were either left untreated or exposed to 3-NPA for 12 hours prior to the assay. The bar graph summarizes changes in complex II OCR of permeabilized B-LCLs from PPBL patients (n = 3) following treatement with 3-NPA. *Right panel:* Production of IL-6 by B-LCLs from PPBL patients (n = 3), measured in the culture supernatant of non-activated cells or cells activated with IL-21 plus CD40L, in the presence or absence of 3-NPA for 48 hours. IL-6 ratios were calculated relative to baseline (untreated cells). IL-6 production from B-LCL of each PPBL patient was tested 2-3 times. (**b**) *Left panel:* Immunoblot analysis of total cell lysates from B-LCLs of PPBL patients (n = 3) transfected with control siRNA, or *SDHA* siRNA, and probed for SDHA protein abundance. The bar graph summarizes knockdown efficiency in B-LCL from PPBL patients (n = 3). Each patient cell line was tested 3 times. *Middle panel:* Representative mitochondrial respiration profile of permeabilized B-LCLs from a PPBL patient prior to and following addition of complex II specific substrates and the SDHA inhibitor, malonate, as indicated (dashed lines). B-LCLs were treated with either control siRNA or *SDHA* siRNA prior to the assay. The bar graph summarizes changes in OCR of permeabilized control siRNA or *SDHA* siRNA treated B-LCLs from PPBL patients (n = 3). *Right panel:* Production of IL-6 by B-LCLs from PPBL patients (n = 3) was quantified in cell culture supernatants of cells that were transfected with control siRNA or *SDHA* siRNA, and cultured for 48 hours. Each patient cell line was tested 2-3 times. (**c**) *Left panel:* Immunoblot analysis of total cell lysates from B-LCLs derived from marginal zone-like B cells from HCs (n = 3) transfected with control siRNA, or fumarate hydratase (FH) siRNA, and probed for FH protein abundance. *Middle panel:* Abundance of fumarate in control siRNA, or FH siRNA treated B-LCLs. The bar graph summarizes fumarate abundance (n = 3). *Right panel:* Production of IL-6 by marginal zone-like B-LCLs from HCs (n = 3) was quantified in cell culture supernatants of cells that were transfected with control siRNA FH siRNA, and cultured for 48 hours. (**d**) SDHA (A45T) (identified in Patient #8) was introduced site-specifically by CRISPR-Cas9 editing in one allele of B-LCLs derived from HC marginal zone-like B cells. Complex II specific respiration was then determined in the non-mutated and in the edited cell line (*left panel:* representative metabolic flux experiment, *middle panel:* summary of complex II specific OCRs), and IL-6 was quantified in the supernatant of both cell populations after 48 hours of cell culture (*right panel*). (**e**) Time per interaction between SDHA and SDHB, calculated as area under the curve (AUC), of each individual simulation replica (wt vs. A45T). (**f**) Molecular representation of the 'SDHA (green) SDHB (blue)' complex, shown in ribbons. The prosthetic group flavin adenine dinucleotide (FAD) is shown as sticks and CPK colored (black arrowhead). A typical snapshot taken from the A45T trajectory is shown. Residues of the N-ter of SDHA within 2.5 Å of SDHB are shown as sticks and CPK colored.

Pooled data are shown as mean ± SEM. Statistical significance was assessed by paired t-test (**a**, **b**), and one-way ANOVA (**e**). * $p < 0.05$, ** $p < 0.01$, *** $p < 0.001$. See also **Figure S4**.

Fumarate inhibits KEAP1 and drives Nrf2 dependent transcription of IL-6.

Next we aimed to mechanistically link SDH hyper-function, fumarate accumulation and inflammatory reprogramming of marginal zone-like B cells. Both succinate and fumarate have been assigned important roles in balancing the activity of α-KG in its function as a co-substrate of histone and DNA demethylases[29,30]. In human monocytes, fumarate accumulation through glutaminolysis inhibits histone demethylation, which has been shown to be the epigenetic basis of augmented inflammatory cytokine production upon re-activation (trained immunity)[31]. To test whether in PPBL B cells a transcriptional response similar to that of trained monocytes was induced, we related the PPBL transcriptomes with that of 'fumarate-trained' monocytes (available in the public domain: https://www.ncbi.nlm.nih.gov/geo/query/acc.cgi?acc=GSE86940)[31]. Gene expression profiles did, however, not correlate between these cell types (**Fig. S5a**). Nonetheless, to screen for gross alterations of histone methylation, pan-H3 methylation was assessed between healthy primary B cells and primary PPBL B cells. In line with our finding that the ratio between α-KG and [succinate & fumarate] was not altered between these two cell types (**Fig. 3c**), no difference in pan-H3 methylation was detected (**Fig. S5b**). Irrespective of abundance of other TCA cycle metabolites, succination of proteins by fumarate has been shown to alter protein function in macrophages and T cells[35,36,58], as well as in non-immune cells[59]. Using an antibody recognizing the stable adduct formed by succination, i.e. S-2-(succino)cysteine (2SC), we compared the protein succination profile of healthy primary B cells and primary PPBL B cells. Indeed, succination was more pronounced in PPBL B cells, with the most prominent band appearing at a size between 60-70 kD (**Fig. 6a**). In cancer cells with loss-of-function mutations in FH, and consecutive accumulation of fumarate, succination of Kelch-like ECH Associated Protein 1 (KEAP1) has been described. Re-probing stripped 2SC immunoblots with a monoclonal antibody against KEAP1 revealed a band at the same position as the prominent 2SC band (**Fig. 6a**). Moreover, succination was also detected on KEAP1 that was immunoprecipitated from PPBL cell lines (**Fig. 6b**). Together, these findings did provide evidence that a fraction of KEAP1 is succinated in PPBL

B cell lines. Constitutive binding of KEAP1 to nuclear factor erythroid 2-related factor 2 (Nrf2) targets the molecule for ubiquitin-dependent degradation[60,61]. A direct consequence of KEAP1 succination is the destabilization of KEAP1-Nrf2 interaction and subsequent nuclear translocation of Nrf2 and transcription of target genes[37,62]. To investigate the activation status of KEAP-1–Nrf2 in marginal zone-like B cells from healthy donors vs. primary B cells from PPBL patients, we stained for KEAP1 in both cell populations and assessed expression by imaging flow cytometry. KEAP1 was more diffused and homogenously distributed in B cells from healthy donors, whereas KEAP1 localization in PPBL B cells was sequestered to a specific cytoplasmic region (**Fig. 6c**). Inhibition of KEAP1 e.g. by succination – which releases Nrf2 – could result in p62-mediated targeting of KEAP1 for autophagosomal degradation[63]. Indeed, in two independent affinity purification experiments that used overexpressed FLAG-tagged KEAP1 as bait, p62 was enriched, which indicated increased interaction between both proteins (data not shown). Together these findings indicated inactivation and autophagosome-targeting of KEAP1 in PPBL B cells, aligning with increased Nrf2 activity. Next, we determined whether pharmacologic stabilization of the KEAP1–Nrf2 interaction impacted production of IL-6 in PPBL B cell lines. K67 is a KEAP1 activator that is dependent on p62 phosphorylation to exert its function. Immunoblots of PPBL B cell lines revealed p62 phosphorylation at basal (as well as activated) conditions (**Fig. 6d**, left panel). Stabilizing KEAP1 following K67 treatment reduced IL-6 output in PPBL B cell lines (**Fig. 6d**, right panel). We then directly assessed the abundance of Nrf2 in the nuclear fraction of marginal zone-like B cell lines from healthy donors vs. that of B cells lines from PPBL B cells. Nrf2 was more abundant in nuclei extracted from PPBL B cell lines (**Fig. 6e**). Moreover, we also tested the sensitivity of Nrf2 nuclear localization to KEAP1 activity. Exposure of primary PPBL B cells to K67 reduced nuclear accumulation of Nrf2 (**Fig. S5c**). To test whether canonical Nrf2 targets were induced in PPBL B cells we first performed a GSEA for the Nrf2–anti-oxidant response pathway. No global enrichment for Nrf2 targets was detected (data not shown). Quantification of transcripts for prototypical Nrf2 target genes by qPCR, however, suggested slightly higher abundance of these gene products in PPBL B cell lines as compared to marginal zone-like B cell lines from healthy donors (**Fig.**

S5d). Next, we further investigated the impact of a direct Nrf2 inhibitor, ML-385 on IL-6 production in PPBL B cell lines. ML-385 is a highly specific Nrf2 inhibitor that was developed for use in patients suffering from cancers with loss-of-function mutations in KEAP1, or gain-of-function mutations in Nrf2[64-66]. Indeed, IL-6 production was reduced in non-activated and activated PPBL B cells following treatment with ML-385 (**Fig. 6f**). Additionally, ML-385 also largely abrogated monomethyl fumarate-driven production of IL-6 (**Fig. S5e**). Together these data argued for low-level canonical (reflected in transcription of NQO1, GCLC, GCLM, THNRD1), and non-canonical (reflected in transcription of IL-6 and IL-8) Nrf2 activity occurring in PPBL B cells. Aligning with these findings, using a computational approach, we identified Nrf2 binding motifs in the promotor regions of IL-6, IL-1β and IL-8 (**Tbl. S3**). To further experimentally explore the occurrence of non-canonical, inflammatory Nrf2 activity in PPBL B cell lines, we (i) reduced Nrf2 protein expression using siRNA technology and (ii) investigated binding of Nrf2 to the IL-6 promotor region, using ChIP PCR. Reducing Nrf2 protein robustly reduced production of IL-6, both at the mRNA and the protein level, in PPBL B cell lines from all three patients (**Fig. 6g**). Also, using ChIP-PCR, Nrf2 binding at two of the predicted binding sites in the IL-6 promoter was increased in PPBL B cell lines, as compared to marginal zone-like B cell lines from healthy donors (**Fig. 6h**, left panel). Binding of Nrf2 to the promoter of NQO1 – by contrast – was comparable in both cell lines (**Fig. 6h**, right panel). Lastly, to assess the potential role of Nrf2 also in the response of primary human B cells, naïve and memory B cells were stimulated with CpG for 24 h. In naïve B cells from healthy donors, inhibition of Nrf2 blunted IL-6 production, with only a slight effect observed in memory cells (**Fig. S5f**, upper panel). Further, there was no appreciable effect on the surface expression of CD69, CD86, HLADR, and CD71 following inhibition of Nrf2 activity in CpG stimulated cells (**Fig. S5f**, lower panel). Notably, however, activation of KEAP1 with K67 did not impact production of IL-6 in these cells, in line with a potentially distinct role for KEAP1-p62 interactions in TLR stimulated primary B cells[67].

Together these data established that excess production of IL-6 in PPBL B cells was mediated by triggering the KEAP1–Nrf2 axis. To test whether blocking IL-6 may have clinical efficacy, we treated

Patient #8 with the IL-6 receptor-blocking antibody, tocilizumab. This clinical intervention was informative in two ways. First, blocking IL-6 was sufficient to abrogate systemic inflammation. This was true for inflammation reflected in a slightly increased CRP, but also BSR, which can result from a plethora of inflammatory stimuli. Second, a clinical questionnaire taken before and two weeks into treatment suggested – at the assumed peak effect of the drug – a beneficial impact of blocking IL-6 signaling in this patient with regard to two difficult to treat symptoms, namely malaise and night sweats (**Fig. 6i**).

Given the newly recognized potential of SDHA to drive an inflammatory immunometabolic axis we went back and interrogated WES data for rare, predicted function-altering variants in SDHA (CADD score >15) among (i) the remainder 11 (i.e. non-PPBL) PAD patients screened metabolically for this study, and (ii) an independent, larger cohort of patients with PAD. In four additional metabolically screened PAD patients we identified rare genetic alterations in SDHA. Among 49 independent further PAD patients, rare genetic variants in the SDHA gene were identified in six (data not shown). Of note, in none of these patients rare variants were observed in the gene encoding for SDHB (data not shown).

Figure 6

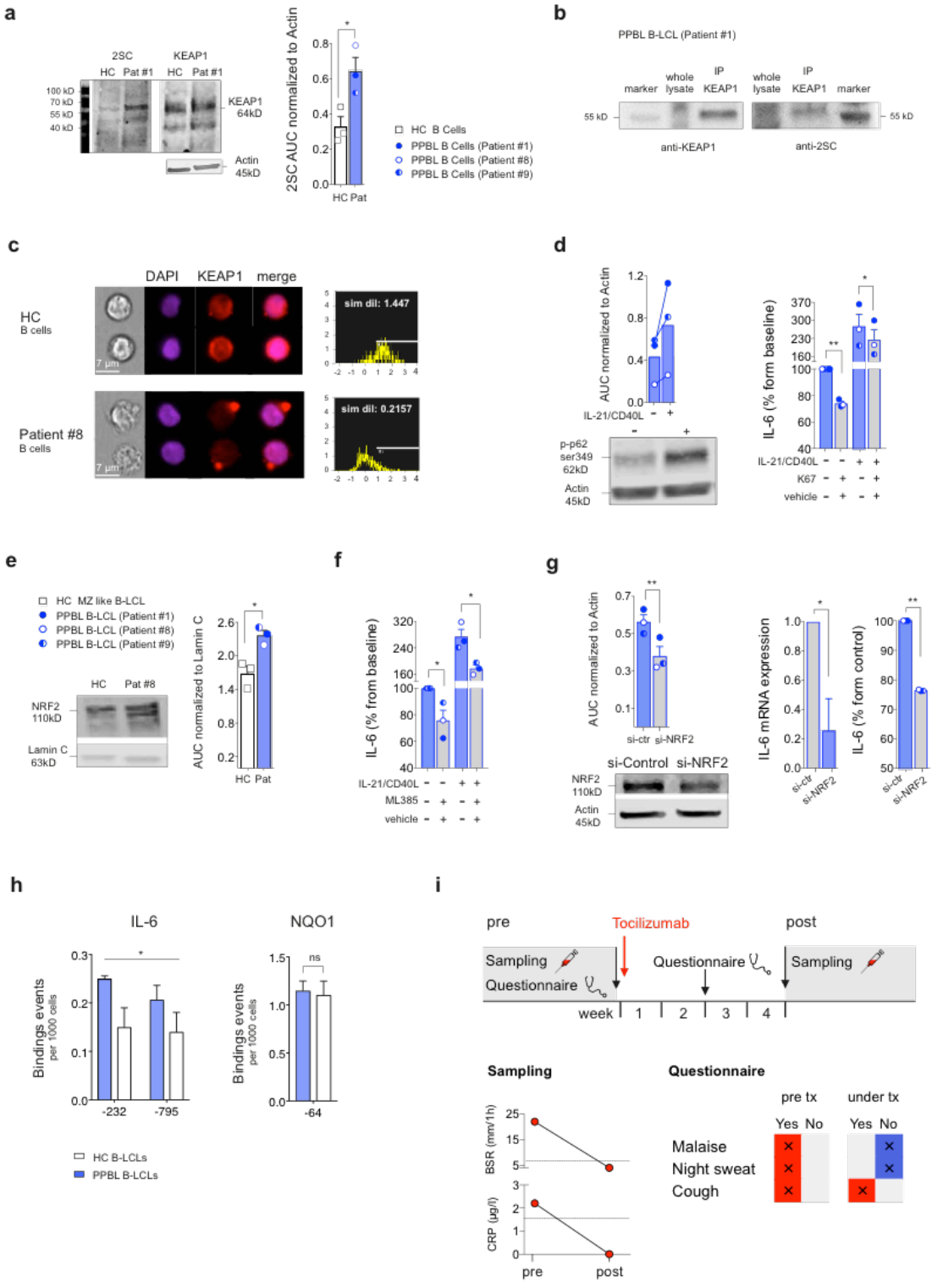
a
2SC
KEAP1
HC Pat #1 HC Pat #1
100 kD
70 kD
55 kD
40 kD
KEAP1 64kD
Actin 45kD
2SC AUC normalized to Actin
HC Pat
HC B Cells
PPBL B Cells (Patient #1)
PPBL B Cells (Patient #8)
PPBL B Cells (Patient #9)
b
PPBL B-LCL (Patient #1)
marker
whole lysate
IP KEAP1
whole lysate
IP KEAP1
marker
55 kD
55 kD
anti-KEAP1
anti-2SC
c
DAPI
KEAP1
merge
HC
B cells
Patient #8
B cells
7 µm
sim dil: 1.447
sim dil: 0.2157
d
AUC normalized to Actin
IL-21/CD40L
p-p62 ser349 62kD
Actin 45kD
IL-6 (% form baseline)
IL-21/CD40L
K67
vehicle
e
HC MZ like B-LCL
PPBL B-LCL (Patient #1)
PPBL B-LCL (Patient #8)
PPBL B-LCL (Patient #9)
HC Pat #8
NRF2 110kD
Lamin C 63kD
AUC normalized to Lamin C
HC Pat
f
IL-6 (% from baseline)
IL-21/CD40L
ML385
vehicle
g
AUC normalized to Actin
si-ctr si-NRF2
si-Control si-NRF2
NRF2 110kD
Actin 45kD
IL-6 mRNA expression
IL-6 (% form control)
si-ctr
si-NRF2
h
IL-6
NQO1
Bindings events per 1000 cells
-232
-795
-64
ns
HC B-LCLs
PPBL B-LCLs
i
pre
Tocilizumab
post
Sampling
Questionnaire
Questionnaire
Sampling
week 1 2 3 4
Sampling
BSR (mm/1h)
CRP (µg/l)
pre
post
Questionnaire
pre tx
under tx
Yes No
Yes No
Malaise
Night sweat
Cough

Legend to Figure 6: Fumarate accumulation, KEAP1–Nrf2 activity and IL-6 production.

(**a**) Representative immunoblot analyses probing primary B cells of HC and PPBL patients for S-(2-succino)cysteine (2SC), followed by stripping and re-staining for KEAP1. The bar graph represents quantification of 2SC abundance at the same height of approx. 64kD in primary B cells of HCs, normalized to actin (n = 3) and PPBL patients (n = 3). (**b**) Representative immunoblot of endogenous KEAP1 immunoprecipitation from PPBL B-LCL. Blots were probed with KEAP1 or 2SC antibodies. (**c**) Representative imaging flow cytometry images of primary bulk B cells from a healthy donor and a PPBL patient. Cells were stained for KEAP1 (red) and a nuclear marker (DAPI, purple). Histograms depict similarity dilate scores of KEAP1 nuclear localization in all cells analyzed. (**d**) *Left panel:* Phosphorylation of p62 was assessed by immunoblotting both in non-activated and activated PPBL B cell lines. A representative blot is shown. *Right panel:* Production of IL-6 by B-LCLs from PPBL patients (n = 3) treated with K67 or with DMSO in the presence or absence of IL-21 plus CD40L for 48 hours. Each patient cell line was independently tested 2-3 times. (**e**) *Left panel:* representative immunoblots of nuclear extracts from B-LCLs derived from healthy donor marginal zone-like B cells or PPBL B cells. Blots were probed with Nrf2 or Lamin C antibodies. *Right panel:* Quantification of Nrf2 nuclear abundance relative to Lamin C from all three PPBL patients. (**f**) Production of IL-6 by B-LCLs from PPBL patients (n = 3), measured in the culture supernatant of non-activated cells, or cells activated with IL-21 plus CD40L, in the presence or absence of the Nrf2 inhibitor, ML-385 or with vehicle (DMSO) for 48 hours. Each patient cell line was tested 2-3 times. (**g**) *Left lower panel:* Representative immunoblot analysis of Nrf2 protein abundance in B-LCLs of a PPBL patient transfected with control or *NRF2* si-RNA. *Left upper panel:* Nrf2 knockdown efficiency quantified across experiments with cells from all three PPBL patients (n = 3). The bar graph summarizes knockdown efficiency of B-LCLs from PPBL patients (n = 3). Each patient cell line was independently tested 2-3 times. *Right panels:* IL-6 transcript abundance and production of IL-6 protein by B-LCLs from PPBL patients (n = 3) either transfected with control si-RNA or *NRF2* si-RNA. Each patient cell line was independently tested 2-3 times. (**h**) Binding of Nrf2 to the IL-6 gene promoter (two predicted binding sites: Tbl. S3) (*left panel*), and the NQO1 gene promoter (*right panel*) in B-LCLs derived from PPBL B cells and healthy donor marginal zone-like B cells. (**i**) *Upper panel:* Schematic summary of the clinical trial performed in Patient #9. *Lower left panel:* CRP and BSR measurements before and under IL-6 receptor blockade. *Lower right panel:* Result of the patient questionnaire filled by the patient.

Pooled data are shown as mean ± SEM. Statistical significance was assessed by unpaired t-test (**a**,**e**,**h** (right panel)), Wilcoxon signed rank test (**f**), paired t-test (**d, g**), and two-way ANOVA (**h**, left panel). * $p < 0.05$, ** $p < 0.01$, ns, not significant. See also **Figure S5**.

In all a molecular framework thus emerged from this study with hyperactive SDH driving accumulation of fumarate, which in turn led to inhibition of KEAP1 likely via succination, with consecutive Nrf2 driven inflammatory, clinically relevant, reprogramming of PPBL B cells (**Fig. S5g**). Whether SDHA gain-of-function, or any other mitochondrial alteration driving accumulation of fumarate, represents a disease modifying inflammatory axis also in other clinical scenarios needs to be investigated.

DISCUSSION

The potential of quantifying lymphocyte metabolic pathway-activities as 'functional biomarkers' of immune dysregulation has not been previously explored. Here, in a prospective screening approach, mitochondrial respiration was found to be higher in B cells from PAD patients. In the subset of patients with the most pronounced respiratory phenotype this observation guided the discovery of a new class of immune-pathologic dysregulation driven by fumarate accumulation. Specifically, hyper-respiration due to SDH gain-of-function mutations was identified as the primary metabolic derangement causative of fumarate accumulation, protein succination and inflammatory reprogramming of marginal zone-like B cells in patients with PPBL. This inflammatory B cell reprogramming aligns with the clinical phenotype observed in these patients. Whether, and if so, *how* hyper-respiration in other (i.e. non-PPBL) PAD patients contributes to specific disease phenotypes remains to be defined. In principle, excess mitochondrial function may link with immunopathology in various ways, ranging from disrupted redox balance or inadequate ROS production to altered acetylation reactions[68,69]; deregulation of epigenetic modifiers and – in light of the findings from this report – pathogenic succination events[18,37,62].

Notably, gain-of-function mutations in proteins of the respiratory chain have not been previously reported – making the here-described SDHA phenotype, and in particular the A45T mutation that we have characterized in detail, the first of its kind. Of note, in PPBL B cells, chronic fumarate-driven production of IL-6 – a key B cell growth factor– may contribute, in addition to driving disease-typic B cell lymphocytosis, to the increased risk for B cell lymphoma noted in these patients[41,70-73]. If indeed overshoot SDH function were linked to tumorigenesis, this would assign this enzyme both tumor suppressing[29,74] *and* tumor promoting properties, since SDH – like several of the respiratory complex-encoding gene products – also has tumor *suppressor* properties[75,76]. Importantly, opportunities to therapeutically target overshoot mitochondrial function may emerge from this insight. In the case of patients with SDHA-driven fumarate accumulation as the metabolic cause for inflammatory

reprogramming, repurposing drugs utilized in cancer patients might become an option. Ionidamine, for example, is a well-tolerated compound that has been shown to inhibit succinate-ubiquinone reductase activity of complex II without fully blocking enzymatic activity[77,78]. In case of succination-dependent activation of the KEAP1–Nrf2 axis, Nrf2 inhibitors might prove successful[64-66]. However, since the KEAP1–Nrf2 axis drives cell-type specific transcriptional responses, mildly targeting the enzyme causative for fumarate accumulation might more precisely affect dysregulated transcriptional responses of marginal zone-like B cells[79].

It is intriguing to note that in multiple sclerosis[80] and psoriasis[81,82], fumarate-esters are being used clinically for their *anti*-inflammatory properties. In macrophages and T cells, pharmacologically increasing fumarate levels has recently been shown to drive succination events, including at the catalytic site of GAPDH[35]. Succination of GAPDH was found to curb aerobic glycolysis in these cells – thereby mediating anti-inflammatory activity[35]. By contrast, we now propose that in PPBL B cells endogenous accumulation of fumarate – via excessive SDH activity – led to succination of KEAP1, which drove a *pro*-inflammatory transcriptional program. As glycolysis was not the driver of the inflammatory output in these cells, PPBL B cells would be predicted to evade GAPDH-directed *anti*-inflammatory activity of fumarate-esters. In fact, exposure of PPBL patients to fumarate-esters might exacerbate inflammation, as suggested by our *in vitro* experiments. This highlights the granularity of immunometabolic regulation and underscores the importance of understanding in detail the distinct metabolic repertoires of normal, as well as pathologic immune cell subsets, as we move towards clinical metabolic interventions.

In mice, marginal zone B cells have been shown to act as innate-like cells with the capacity to rapidly mount a first-line defensive immune response[47]. As such these cells are poised to quickly produce a plethora of inflammatory cytokines. In humans, IgD^+ $CD27^+$ B cells are the assumed counterparts of rodent marginal zone B cells[83]. While the precise functional relevance of human marginal zone-like B cells remains unknown, they also rapidly produce inflammatory cytokines upon stimulation[47,48]. Aligning with the clinical phenotype of the PPBL patients in this study, endogenous fumarate

accumulation did drive a non-regulated inflammatory cytokine output. It is interesting to note that cigarette smoking has been demonstrated to drive up-regulation of OxPhos proteins, including SDHA, and – in line with this – fumarate accumulation was observed in the serum of smokers[84,85]. Smoking, which is highly associated with PPBL is, *per se*, a well-established risk factor for systemic autoimmune diseases, such as lupus erythematosus but also for autoimmune phenomena without overt autoimmune disease[86,87]. Further, smoking has been suggested to increase absolute lymphocyte counts and alter the distribution of B cell subpopulations, which, intriguingly, is also observed upon clinical administration of dimethyl-fumarate[88,89,90]. It thus can be speculated that the activation of the fumarate–KEAP1–Nrf2 axis observed here in cigarette smoking PPBL patients reflects an extreme variant of a much more common, smoking-associated immunometabolic dysregulation.

Also in other contexts marginal zone B cells have been shown to contribute to immunopathology. Specifically, IL-6 produced by marginal zone B cells has been demonstrated to exacerbate experimental systemic inflammatory responses[91]. In the context of autoimmunity, such as Sjogren's syndrome, marginal zone B cells have likewise been proposed to contribute to disease[92,93]. Whether metabolic dysregulation plays a role in the inadequate activation of marginal zone B cells in autoimmunity remains to be assessed.

In each of the study participants with PPBL the genetic analysis identified rare germline mutations in *SDHA*. All three individuals carried, however, different mutations. For the A45T mutation (Patient #8) we provide direct experimental evidence (**Fig. 5d**) and detailed structural modeling (**Fig. S4d-f**, and **Fig. 5e,f**). *In silico*, the Thr at position 45 of the mutated SDHA contributed to only a small amount of inter-domain contacts, which did not support the hypothesis of a direct interaction between this residue and SDHB as the mechanism causing enhanced interactions between the two proteins. Instead, the data suggest that Thr at position 45 stabilizes interactions between SDHA and SDHB by engaging with residues on the adjacent surface of SDHA, specifically Arg458, Phe459, Asp511, Arg512 and Met514. Such binding maintains the N-ter segment of SDHA at the interface to SDHA in a position facilitating formation of hydrogen bonds between the N-ter of SDHA and residues Asp20 and Asp22 of

SDHB[92]. How the mutation we detected in Patient #9 and #15 imposed SDHA gain-of-function at the molecular level remains to be determined. The same is true for the mutation identified in Patient #1, which was synonymous. The mutation was not at a splice site and it did not detectably affect protein expression (**Fig. S2c**, **Fig. 2d**). Synonymous mutations were long believed to be functionally neutral. However, there is increasing evidence to the contrary. Indeed codon usage bias, i.e. unequal frequency at which synonymous codons are found, has been demonstrated in most genomes at above random levels[94]. Importantly, synonymous rare codons have also been shown to play important functional roles in e.g. regulation of co-translational folding and covalent modifications, *in vivo*[95]. While much remains to be learned about the molecular events that connect synonymous codon usage, protein biogenesis and cell physiology, the here identified mutation might be subject to one such mechanism. The functional and clinical importance of synonymous mutations in human disease is underscored by the fact hat more than 50 human pathologies firmly associate with them, and that – overall – non-synonymous and synonymous mutations have a similar probability of associating with disease[96,97].

In summary, instructed by metabolic screening, this study identified SDHA gain-of-function as a novel primary immune dysregulation, driving fumarate accumulation, succination and inflammatory reprogramming of marginal zone-like B cells. Representing the first example of a *primary retrograde signaling pathology* (i.e. disruption of mitochondria-to-cellular-transcriptional regulation), our data point to therapeutic repurposing-strategies by uncovering druggable targets – namely SDHA, Nrf2 and IL-6 – along this dysregulated molecular axis.

MATERIALS AND METHODS

Study subjects

The study was approved by the *Ethikkommission Nordwest- und Zentralschweiz* (EKNZ 2015-187); complied with all relevant ethical regulations, and informed consent was obtained from all participants. Fourteen patients, and 15 age and sex matched healthy controls, were prospectively recruited between July 2015 and December 2016. One additional PPBL patient was recruited 2018. Inclusion criteria for patients were as follows: Age >18 years; serum IgG level <7g/l, or IgG subclass deficiency (IgG_1 <4.9 g/l, IgG_2 <1.5 g/l, IgG_3 <0.2 g/l, IgG_4 <0.08 g/l). Patients evaluated by a Clinical Immunologist and classified as having a form of secondary antibody deficiency were excluded from the study.

Blood sample routine phenotyping and immunoglobulin quantification

After written informed consent, blood samples from patients and healthy controls (Blood donor Center, University Hospital Basel) were obtained. From all patients a differential white blood cell count, including total lymphocyte as well as T and B cell absolute numbers, were obtained. B cells ($CD19^+$ in lymphocyte gate) were further phenotyped as follows: naïve B cells ($IgD^+CD27^-IgM^+$), marginal zone-like B cells ($IgD^+CD27^+IgM^+$), memory B cells ($IgD^-CD27^+IgM^-$), transitional B cells ($IgD^+IgM^+CD38^+$), CD21 low B cells ($CD21^{low}CD38^-$), and plasmablasts ($IgD^-IgM^-CD38^{++}$). T cells ($CD3^+$ in lymphocyte gate) were classified into: $CD4^+$ T cells, $CD8^+$ T cells, naïve ($CD27^+CD45RO^-$) vs. central memory ($CD27^+CD45RO^+$) vs. effector memory ($CD27^-CD45RO^{+/-}$). Serum levels of total IgG and IgG subclasses (IgG_{1-4}); IgM; IgA (data not shown), and IgE (data not shown) were quantified. All above experiments were performed at the GMP-certified central laboratory of the University Hospital Basel.

Cell sorting and phenotyping

To obtain immune cell subsets, peripheral blood mononuclear cells (PBMCs) were first isolated by standard density-gradient centrifugation (Lymphoprep Fresenus Kabi, Norway). B cells ($CD19^+$) and T cells ($CD3^+$) were then positively selected using magnetic beads (Miltenyi Biotec, Germany) according to the manufacturer's instructions. For isolation of marginal zone-like B cells, B cells ($CD19^+$) were stained with anti-CD27 brilliant Violet 605 (O323) (Biolegend, USA) and anti-IgD VioBlue (REA740, Miltenyi Biotec) mAb. $CD19^+$ $CD27^+$ IgD^+ B cells were sorted with a BD Influx cell sorter (BD Bioscience, USA). Prior to downstream experiments, cells were rested for 3 hours in RPMI-1640 medium (GIBCO, USA) containing 10% fetal bovine serum (FBS, GIBCO, USA), 50U/ml penicillin and 50 μg/ml streptomycin (GIBCO) (R10-FBS) at 37°C. FACS sorted naïve and memory B cells (as above) were activated with CpG (2.5 μg/ml) for 24 hours and then stained with anti-CD86-PE (IT2.2, Biolegend), anti-CD69-FITC (FN50, Immunotools), anti-HLADR-APC (G46-6, BD Biosciences), and anti-CD71-PE (CY1G4, Biolegend). For carboxyfluorescein succinimidyl ester (CFSE) dilution assays, PBMCs were stained with CFSE and then activated with anti-CD3 and anti-CD28 mAb (for T cells), or with CpG or IL-21/CD40L (for B cells). Cells were stimulated for 5 days and then assessed by flow cytometry. For CMV ELISPOT assays patient and healthy control PBMCs were stimulated CMV antigens using the T-track CMV kit (Lophius) and assessed for IFN-γ production by using a spot reader (AID). For detailed B cell phenotyping the following additional antibodies were used: anti-CD24 (IML5, Biolegend), anti-CD38 (HIT2, BD Biosciences), anti-TACI (1A1, Biolegend).

EBV transformed B lymphocyte cell lines

PBMCs or sorted marginal zone-like B cells were incubated with EBV-containing supernatant from B95-8 cells for 1 hour and additionally stimulated with CpG (1 μg/ml). Cyclosporine A (1 μg/ml) was added weekly for a total of four weeks to eliminate T cells. Purity of EBV transformed B cell lines, as defined by flow cytometry, was 92-98 % ($CD19^+$ $CD3^-$).

Metabolic flux analysis

A Seahorse XF-96^{e} extracellular flux analyzer (Seahorse Bioscience, Agilent Technologies, USA) was used to define oxygen consumption rates (OCR) and extracellular acidification rates (ECAR). Cells were plated ($3x10^5$ cells/well) onto plates coated with Cell-Tak (Corning, USA). Mitochondrial perturbation experiments were carried out by sequential addition of oligomycin (1 μM, Sigma-Aldrich, USA), FCCP (2 μM, Carbonyl cyanide 4-(trifluoromethoxy) phenylhydrazone, Sigma-Aldrich), and rotenone (1 μM, Sigma-Aldrich). OCR and ECAR values were monitored in real time after injection of each compound. Basal respiration was calculated by subtracting non-mitochondrial respiration (post rotenone-rate) from baseline rate[27]. For measuring activation-induced glycolytic activity, primary B cells were activated with IL-21 (200 ng/ml, ImmunoTools, Germany) and CD40L (200 ng/ml, Sigma-Aldrich) injected into the metabolic flux analyzer via injection ports, and ECAR was monitored in real time. For monitoring OCR of intact mitochondria only, cells were resuspended in MAS buffer (70 mM sucrose, 220 mM mannitol, 10 mM KH_2PO_4, 5 mM $MgCl_2$, 2 mM HEPES, and 1 mM EGTA), then treated with the XF plasma membrane permeabilizer (Seahorse, Agilent Technologies), which was followed by addition of pyruvate (5 mM) / malate (2.5 mM) / ADP (1 mM) and rotenone (1 μM) for monitoring complex I-driven respiration; succinate (10 mM) / ADP (1 mM) with/without rotenone (1 μm / 2 μm) and malonate (0.04 mM) for monitoring complex II-driven respiration; duroquinol (0.5 mM) / ADP (1 mM) and antimycin A (0.02 mM) for monitoring complex III-driven respiration; TMPD (0.5 mM) / Ascorbate 2 mM) / ADP (1 mM) and sodium azide (20 mM) (all from Sigma-Aldrich) for monitoring complex IV-driven respiration. Changes in OCR upon substrate addition were calculated relative to the pre-injection rate.

2-NBDG uptake

To assess glucose-uptake, $5x10^5$ primary B cells were activated with IL-21 (200 ng/ml, ImmunoTools) and CD40L (200 ng/ml, Sigma-Aldrich) for 24 hours. Cells were then incubated in medium containing 20 µM 2-NBDG (Invitrogen) for 45 min and analyzed by flow cytometry.

Electron microscopy

Transmission electron microscopy was performed at the Biozentrum (University of Basel). Primary B cells were sequentially fixed in 3% paraformaldehyde, 0.5% glutaraldehyde and 1% osmium tetraoxide, embedded and then cut into 60 nm sections. Micrographs (27'000x magnification) were obtained with a Morgagni 268 (FEI, Hillsboro OR, USA) transmission electron microscope operated at 80 kV. ImageJ software (NIH, Bethesda, USA) was used for measuring cell area; mitochondrial area, and mitochondrial length (major axis) and width (minor axis). The aspect ratio of mitochondria was calculated as 'major axis' over 'minor axis', an aspect ratio of 1 indicating a circular mitochondrial section.

Isolation of mitochondria

Cell pellets were washed with cold PBS and lysed using RIPA buffer (Thermo Fisher Scientific, Rockford IL, USA) containing protease and phosphatase inhibitors (Roche, Switzerland). To prepare mitochondrial fractions, $3x10^7$ B-LCLs were collected and washed with buffer A (83 mM sucrose, 10 mM MOPS, pH 7.4). Cell pellets were then homogenized with 20 strokes in a tightly fitting glass-teflon homogenizer with 1 ml of buffer B (buffer A plus 10mM triethanolamine, 5% percoll, 0.01% digitonin, proteaseinhibitor, pH 7.4). Nuclei and unbroken cells were removed by centrifugation at 2'500 x *g* for 5 min. Supernatants were collected and centrifuged at 10'000 x *g* for 15 min. Mitochondria were then suspended in an appropriate volume of buffer C (300 mM sucrose, EGTA 1 mM, 20mM MOPS, proteaseinhibitor, pH 7.4) for storage at −80°C until use.

Immunoblot analysis

Protein concentrations were determined by BCA protein assay kit (Thermo Fisher Scientific). Whole-cell lysates or mitochondrial fractions were separated by 4-15% Mini Protean TGX Gel (Bio-Rad, Hercules CA, USA), and transferred to nitrocellulose using Trans-Blot Turbo Transfer (Bio-Rad, Hercules CA, USA). Membranes were probed with anti-Grim19 mAb (ab110240), anit-NDFU8 mAb (ab110242), anti-SDHB mAb (ab14714), anti-Complex III subunit Core 2 mAb (ab14745), anti-Complex IV subunit II mAb (ab110258) and anti-ATPα mAb (ab14748) (all from Abcam), anti-SDHA mAb (119989), anti-FH mAb (4567), anti-KEAP1 mAb (8047), anti-Nrf2 pAb (12721), pan-methyl-histone H3 (Lys9) mAb (4473) and anti-β-actin mAb (3700) (all from Cell Signaling, USA) and anti-2SC pAb (crb2005017e, Cambridge Research Biochemicals, UK). Blots were then stained with the appropriate secondary antibody (IRDye 800CW-conjugated goat polyclonal antibody against rabbit IgG (926-32211) or RDye 800CW-conjugated goat polyclonal antibody against mouse IgG (926-32219) from LI-COR). The Odyssey imaging system (LICOR) was used for detection, and the ImageJ software (1.48v) for quantification.

Blue native PAGE

For isolation of mitoplasts, 8 x 10^6 B-LCLs were re-suspended in 100 µl of PBS, 32.5 µl of digitonin (8 mg/ml) was added and cells were incubated on ice for 10 min. Cold PBS (1 ml) was added and cells were centrifuged for 5 min at 10'000 x *g*. The pellet was resuspended in 100 µl of AA buffer (500 mM 6-aminohexanoic acid, 50 mM immidazole, 1 mM EDTA, pH 7) and 10 µl of a 10% digitonin solution was added. Next, cells were centrifuged for 30 min at 18'000 x *g*. Supernatant was harvested and 10 µl of sample buffer (5% blue G-250, 5% glycerol in AA Buffer) was added. Samples were stored at -80°C until use. BN-PAGE was performed as described[98]. Membranes were probed for anti-NDUFA9 mAb (20C11B11B11, Abcam), anti-complex II 70 kDA Fp mAb (459200, Invitrogen), Anti-UQCRC1 mAB (16D10AD9AH5) (110252, Abcam), anti-oxphos Complex IV

Subunit I mAb (459600, Invitrogen), anti-ATPB antibody [3D5] - Mitochondrial Marker mAb (14730, Abcam) and Tomm20 (FL-145) (sc11415, Santa Cruz Biotechnology, USA). For densitometry analysis, the ImageJ64 software was used. Band limits were determined using low-exposure images to efficiently distinguish individual bands.

Mitotracker red and mitotracker deep red staining

Primary B cells were incubated for 20 min at 37°C / 5% CO_2 with 100 nM Mitotracker red (MTR, Invitrogen), or 100 nM Mitotracker deep red (MTDR, Invitrogen), respectively. Cells were then washed twice in staining buffer (PBS plus 1% bovine serum albumin) and analyzed by flow cytometry.

Activity of individual respiratory chain complexes

To measure the activity of individual mitochondrial respiratory chain complexes, ELISA microplate assay kits (Abcam, UK) were used according to the manufacturer's instructions. In brief, complex I activity was analyzed by tracking oxidation of NADH; complex II by via the production of ubiquinone; complex IV by tracing oxidation of cytochrome c; complex V by assessing conversion of ATP to ADP and the coupled oxidation of NADH.

Metabolomics

Cells from primary patient B cells and primary marginal zone-like B cells from healthy controls were isolated as described above, washed twice with cold PBS, snap frozen in EtOH containing dry ice and stored at −80°C. Metabolomic assays and analysis were performed by Metabolon Inc. (Durham, USA). For in-house targeted metabolomics assays, cells were counted, adjusted to 6 x 10^6 per sample, washed with ice-cold PBS and counted again with a CASY cell counter. Metabolites were extracted with 350 µl of 80:20 Methanol:water. Samples were centrifuged (3220x *g* for 30 min at 10°C) and 5 µl was injected into the LC-MS/MS system. Mass spectrometry was performed on an ultra-high-pressure

liquid chromatography (UHPLC) system from Shimadzu (Kyoto, Japan), which was connected to an API-4000 Qtrap triple quadrupole mass spectrometer (AB Sciex, Concord, Canada). A Symmetry C18 (3.5 uM, 4.6 x 75mm, Waters) column was used to separate succinate and fumarate. Mobile phase A consisted of water supplemented with 0.1 % formic acid, while acetonitrile with 0.1 % formic acid was used as mobile phase B. Baseline separation was achieved using a stepwise gradient program. Mobile B at 30 % from 0-1 min; mobile B 30 % to 95 % from 1-2 min; mobile B 95 % from 2-3 min; mobile B 30 % from 3-3.5 min. Importantly, these settings enabled the separation of methylmalonate from the isobaric succinate. The two metabolites succinate and fumarate were analyzed by electrospray ionization in the negative mode using multiple reaction monitoring. The LC-MS/MS system was operated and samples were quantitated with Analyst software 1.6.2 (AB Sciex, MA, USA).

$^{13}C_6$ glucose and $^{13}C_6$ glutamine tracing

Primary B cells ($2x10^6$) from patients were plated onto 48 well plates in RPMI10-FBS with 4 mM U-^{13}C glucose or 4 mM U-^{13}C glutamine for 6 hours. Metabolites were extracted with 50 % MeOH / 30 % Acetonitrile. Isotopologue distribution was assessed by GC-MS. Metabolites were extracted from cells using ice-cold 80 % methanol, followed by sonication and removal of cellular debris by centrifugation at 4°C. Metabolite extracts were dried, derivatized as tert-butyldimethylsilyl (TBDMS) esters, and analyzed via GC-MS as previously described[99]. Uniformly deuterated myristic acid (750 ng / sample) was added as an internal standard following cellular metabolite extraction, and metabolite abundance was expressed relative to the internal standard, and normalized to cell number. Mass isotopomer distribution was determined using a custom algorithm developed at McGill University, Canada[100].

RNA sequencing

RNA from primary patient B cells and primary marginal zone-like B cells from healthy controls was isolated using nucleospin RNA kit (Macherey-Nagel, Germany) following manufacturer's instructions.

RNA-seq was performed by Admera Health (USA). In brief, samples were isolated using ethanol precipitation. Quality check was performed using Tapestation RNA HS Assay (Agilent Technologies, USA) and quantified by Qubit RNA HS assay (Thermo Fisher Scientific). Ribosomal RNA depletion was performed with Ribo-zero Magnetic Gold Kit (MRZG12324, Illumina Inc., USA). Samples were randomly primed and fragmented based on manufacturer's recommendation (NEBNext® Ultra™ RNA Library Prep Kit for Illumina®). First strand was synthesized using Protoscript II Reverse Transcriptase with a longer extension period (40 min for 42°C). All remaining steps for library construction were used according to the NEBNext® Ultra™ RNA Library Prep Kit for Illumina®. Illumina 8-nt dual-indices were used. Samples were pooled and sequencing on a HiSeq with a read length configuration of 150 paired-end.

Whole exome sequencing

The Oragene DNA OG-500 kit (DNA Genotek Inc., Canada) was used to collect saliva from patients, DNA was extracted using PrepIT L2P reagent (DNA Genotek Inc.). Whole exome sequencing (WES) was performed on B cells, T cells and saliva of all 3 PPBL patients included in this study. The input DNA concentration was 200 ng. DNA was quality controlled using Genomic DNA ScreenTape System (200 bp to 60000 bp) on a TapeStation 2200 (both Agilent Technologies). Sonication with a Covaris E220 was used to achieve fragmentation to 150-200bp. Sonication as well as library preparation was performed using the SureSelectXT Target Enrichment System for Illumina Paired-End Sequencing Library Protocol (Version C0, December 2016). SureSelectXT Reagent kits were used for library preparation (Agilent Technologies).

Exon-specific biotinylated oligonucleotides, SureSelect Human All Exon V6 (Agilent Technologies), were hybridized with the samples. Exons were pulled down using Dynabeads MyOne Streptavidin T1 magnetic beads (Thermo Fisher Scientific). Paired-end 125 bp sequencing was performed on HiSeq 4000 Illumina platform. Output files from the sequencer were in FASTQ format. Paired-end sequencing

resulted in two FASTQ files for each sample, forward and reverse. Forward and reverse FASTQ files were aligned to the reference genome (hg19) using Burrows-Wheeler Aligner. The output of BWA was a sequence alignment map (SAM) file. Picard tools v2.7.1 was used to make a binary version of SAM files (=BAM files). Quality control was performed as per Genome Analysis Tool Kit (GATK) v3.5 guidelines from Broad Institute[101]. Each output BAM file was individually analyzed for variants from the reference genome using HaplotypeCaller from GATK resulting in a variant called file (VCF). Annotation of mutations was performed using Combined Annotation Dependent Depletion (CADD v1.3) and Variant effect predictor (VEP) programs[102,103]. Mutations of interest were visualized *in silico* using the Integrative Genomics Viewer (IGV) in order to confirm the mutation was in fact somatic and not present in controls[96,104]. The synonymous mutation was further investigated for splice altering, miRNA site, or mRNA structure altering, using NNSplice, Human Splicing Finder, TargetScan and Rescue ESE[105,106]. Somatic analysis was performed using VarScan v2.3.9[107], Strelka Somatic Caller and MuTect2[108,109]. Annotation of somatic mutations from the 3 callers was performed using CADD v1.3 and VEP programs. Somatic mutations were visualized *in silico* using IGV.

Cytokine measurements

B-LCLs (4×10^6) from patients, and marginal zone-like B-LCLs from healthy controls, were plated into 48 well plates. Cells were either left unstimulated (non-activated controls), or activated with IL-21 (40 ng/ml, ImmunoTools) and CD40L (40 ng/ml, Sigma-Aldrich). As indicated, 3-NPA (1.5 μM, Sigma-Aldrich), ML-385 (5 μM, Sigma-Aldrich), SML-1922 (50 μM, Sigma-Aldrich) or monomethyl fumarate (25 μM) was added. Supernatants were harvested 48 hours after activation, and concentrations of IL-6 was measured using Legendplex, human multiplex Panel (Biolegend), according to the manufacturer's instructions.

RNA mediated interference

B-LCLs ($2x10^6$) from patients, and marginal zone-like B-LCLs from healthy controls, were transfected with pools of siRNA targeting *SDHA*, *NRF2*, or control scrambled siRNA (each 30 pmol) (QIAGEN) and rested for 48 hours, using the AMAXA cell line V nucleofection kit (Lonza). Knockdown efficiency was assessed by immunoblot analyses of the respective proteins.

CRISPR-editing

Introduction of the SDHA A45T point mutation into B-LCLs from healthy marginal zone-like B cells was performed by Genoway. Briefly, to introduce SDHA A45T point mutations into B-LCLs from healthy marginal zone like B-LCLs, the CRISPR/Cas9 system was used. Cells were transfected with a single vector that contained Cas9, gRNA and a small single-stranded oligonucleotide (ssODN) that encoded the point mutation. Using this technique heterogenous cell lines from three separate experiments were generated. These heterogenous cell lines contained cells with the expected SDHA A45T point mutation at a single allele or cells with only wild type alleles. No additional insertions/deletions were detected.

Molecular dynamics simulation

Interaction between SDHA and SDHB were studied using MD simulations. To date no structures of human SDHA or SDHB have been published, yet the crystal structure of porcine heart mitochondrial complex II has been solved at 3.1 Å resolution (PDB code 4YTP)[110]. Porcine SDHA shares 94.58% protein identity with its human homolog (P31040), and the porcine and human SDHB proteins share high sequence homology as well. To generate a model of the human SDHA/SDHB complex, the sequence of the protein, as obtained from the US National Centre for Biotechnology Information (https://www.ncbi.nlm.nih.gov - accessed 22nd February 2018), was submitted to the automated protein structure homology-modeling server, SWISS-MODEL[111]. Using the VMD[112,] and Chimera suites[113], a complex of human SDHA and SDHB was designed as follows: the N-ter SDHA segment was

generated and grafted onto the SDHA structure as well the C-ter and both termini of SDHB. Using VMD, the 20 residues of the porcine SDHA/SDHB that differ from the human protein were changed into the corresponding human counterparts. Finally, two different models were generated, each extended at the N-ter with segments of sequence ASAKVSDSI (wt) and ASTKVSDSI (A45T mutation), respectively[112,114], SDHA contains the prosthetic group flavin adenine dinucleotide (FAD), SDHB three iron-sulphur clusters. The structure of FAD was obtained from the Zinc library and their parameters were calculated through the CHARMM General Force Field (CGenFF) version 1.0.0.[115,116]. To study the SDHA-SDHB interaction, the FAD prosthetic group and the residues located in the cores of the subdomains were simulated with position restraints (with a force constant of 400 kJ mol^{-1} nm^{-2}). The proteins, including FAD, were virtually inserted in a water box, and K^+ and Cl^- ions added to simulate a physiological ionic concentration of 150 mM, and their respective number set to neutralize the system. Simulations were conducted with the GROMACS package, version 2016.3[117], using parallel tempering. The CHARMM36 topology and parameter files were used to represent the protein and water was represented by the TIP3P model, whereas parameters for FAD were calculated with CGenFF[115,118]. The calculation of the electrostatic forces utilized the Particle-Mesh Ewald summation method, with a cutoff of 12 Å for the real space interactions, a 1.2 Å grid and 4^{th} order spline interpolation for the reciprocal space. The Lennard-Jones short and long-range cutoffs were set to 12 Å and 10 Å, respectively. Isotropic pressure at 1 bar was virtually maintained through coupling to a Parrinello-Rahman barostat[119], with a virtual compressibility of 4.5 x 10^{-5} bar and a coupling time of 5 ps. Prior to the simulations, the systems were minimized with steepest descent. In order to further equilibrate the systems and allow water molecules to relax, a 25 ps simulation with a time step of 1 fs and with position restraints on the protein atoms was performed (with a force constant of 400 kJ mol^{-1} nm^{-2}). For parallel tempering, an ensemble of 48 temperatures in the range 310-385K was generated, whereas solute and solvent were weakly coupled to Nose-Hoover[120] thermostats with coupling times of 1 ps[121,122]. Bonds with hydrogen atoms were constraint using the LINCS algorithm allowing usage of a time step of 2 fs. An interval of 0.4 ns was set for the exchange probability calculation, thus providing

enough time for SDHA-SDHB interactions to occur. Each individual trajectory was ~22.5-23.0 ns long, totalizing 1100 and 1080 ns for the wt and the A45T mutant, respectively. The trajectories simulated for at a temperature lower than 360K were retained for the analyses, which were conducted either on the statistical platform R and specific R packages, GROMACS tools, or in-house Python scripts[123]. The readHBmap.py script was used to extract the hydrogen bond existences from the hydrogen bond Map files.

SDHA end point PCR and sequencing

RNA was isolated from B-LCL (5 x 10^6) of patient #8 using Trizol (Thermo Fisher Scientific) and chloroform (Sigma-Aldrich) according to the manufacturer's protocol, then purified with the QIAamp RNA Blood Mini Kit (QIAGEN, Germany). RNA concentration was determined using the NanoDrop 2000c (Thermo Fisher Scientific). DNA digestion was done with DNase I – Amplification Grade Kit (Sigma-Aldrich). 100 ng/µl - 1 µg/µl RNA were used for cDNA synthesis. Random primers (Promega, USA) were annealed at 70°C for 5 min. cDNA synthesis was performed according to the Qiagen's GoScript Reverse Transcription System protocol in a TProfessional TRIO PCR Thermocycler (Core Life Sciences, USA). To search for the mutation in the cDNA of patient #8, primers were designed to amplify a fragment of the *SDHA* transcripts by using the ncbi primer blast web tool (https://www.ncbi.nlm.nih.gov/tools/primer-blast/). The following primers were used: Forward primer: CGA CTC CGG CGT GGT G; Reverse primer: TTT TCT AGC TCG ACC ACG GC. End point PCR was performed using cDNA of B-LCL from patient #8, and Go Taq G2 DNA Polymerase (Promega) with the GoTaq Green Master Mix (Promega) in a TProfessional TRIO PCR Thermocycler (Core Life Sciences). The following thermocycler conditions were used: Initial denaturation 95°C for 2 min, denaturation 95°C for 20 s, primer annealing 63°C for 20 s, elongation 72°C for 1 min, total 34 cycles. PCR products were separated using a 1.5% agarose gel electrophoresis and the band around the expected length of 534 bp was extracted and purified using Qiaquick Gel Extraction Kit (QIAGEN). Extracted DNA was

used for Sanger sequencing, performed by the Sanger sequencing service of the company microsynth (Switzerland). Sequencing results were analyzed using Snap Gene Viewer.

SDHA plus SDHB activity

SDH activity (i.e. compound activity of SDHA and SDHB) was measured spectrophotometrically from the reduction of 2,6-diclorophenol-indophenol (DCPIP) by tracking the absorbance at 600 nm over 3 min. Specifically, frozen B-LCLs (5 x 10^6) were thawed and resuspended in 100 µl PBS on ice, protein concentration was determined, and the volume was adjusted to the sample with the lowest concentration. Each sample (20 µl) was suspended in 950 µl of buffer C1/C2 (25 mM potassium phosphate (K_2HPO_4) (pH = 7.2), 5 mM $MgCl_2$, 3 mM KCN, 2.5 mg/ml BSA) supplemented with 100 mM succinate and 0.1% Triton X-100, and incubated 10 min at room temperature. After addition of 6 µl 5 mM DCPIP, 2 µl 1 mg/ml of antimycin A and 2 µl 1 mM rotenone, samples were incubated for 2 min. Then, 6 µl of 10 mM phenazine methosulfate (PMS) was added and absorbance was measured. Compound activity of SDHA and SDHB was extrapolated using the following formula: [SDH activity = ((rate/min)/19.1) / sample volume x 1000 x dilution factor], where 19.1 is the molar extinction coefficient at 30°C (mM^{-1} cm^{-1}).

Overexpression

B-LCLs were nucleofected (Lonza) with Flag-KEAP1 for 24 or 48 hours. Flag-KEAP1 was a gift from Qing Zhong (UC Berkeley). KEAP1 interacting proteins were purified using anti-FLAG antibodies (clone 9A3, Cell signaling) and identified by affinity purification MS. Transfection efficiency was assessed by Immunoblots.

Imaging Flow cytometry

Primary B cells from healthy controls and PPBL patients were fixed with 4% paraformaldehyde and permeabilized with 0.3% Triton-X 100. Cells were blocked with 5% goat serum and stained with primary antibody (Keap1-mAb Ms, Thermo-Fisher; Nrf2-pAb Rb, Abcam) in blocking medium at 4°C, overnight. Cells were then stained with secondary antibodies (Thermo Fisher) and counterstained with DAPI. Images were acquired using the Imagestream X Mark II imaging flow cytometer (AMNIS). Between 1000-2000 events were collected and imaged at 60x magnification. For analysis, the nuclear localization wizard from the IDEAS software (AMNIS) was used. High similarity dilate mean scores reflect increased nuclear localization. For assessment of Nrf2 nuclear translocation following addition of Keap1 activation, cells were treated with K67 for 24 hours and then fixed for staining as above.

ChIP-PCR

ChIP-PCR was performed by Active Motif. In brief, human B cells were fixed with 1% formaldehyde for 15 min and quenched with 0.125 M glycine. Chromatin was isolated by the addition of lysis buffer, followed by disruption with a Dounce homogenizer. Lysates were sonicated using the EpiShear™ Probe Sonicator (Active Motif) with an EpiShear™ Cooled Sonication Platform (Active Motif) and the DNA sheared to an average length of 300-500 bp. Genomic DNA (Input) was prepared by treating aliquots of chromatin with RNase, proteinase K and heat for de-crosslinking (overnight at 65°C) followed by ethanol precipitation. Pellets were resuspended and the resulting DNA was quantified on a CLARIOStar® spectrophotometer. Extrapolation to the original chromatin volume allowed quantitation of the total chromatin yield. Aliquots of chromatin (25 μg) were precleared with protein A agarose beads (Invitrogen). Genomic DNA regions of interest were isolated using an antibody against NRF2 (Santa Cruz Biotechnologies, cat. no. sc-13032), Complexes were washed, eluted from the beads with SDS buffer, and subjected to RNase and proteinase K treatment). Crosslinks were reversed by incubation overnight at 65°C, and ChIP DNA was purified by phenol-chloroform extraction and ethanol precipitation. Quantitative PCR (QPCR) reactions were carried out in triplicate using SYBR Green

Supermix (Bio-Rad) on a CFX Connect™ Real Time PCR system. The resulting signals were normalized for primer efficiency by carrying out QPCR for each primer pair using pooled input DNA from the samples.

ACKNOWLEDGEMENTS

The authors would like to thank the patients that participated in the study; the flow sorting team and the microscopy core facility of the Department of Biomedicine, University and University Hospital of Basel; the Blood Donor Center affiliated with the University Hospital of Basel, as well as Gideon Hoenger, Urs Duthaler, Claudio Gasser, Julia Hirsiger, Christoph Berger, Thomas Daikeler, Florian Marquardsen and Fabian Baldin for technical support and/or help with the clinical management of patients. Funding: C.H. and M.R. Gebert Rüf Foundation GRS-058/14; C.H. SNSF 31003A_172848; M.R. SNSF PP00P3_172848.

AUTHORS CONTRIBUTION

AVB performed and analyzed most experiments and helped writing the report; GRB performed experiments, conceived, coordinated and supervised the revision experiments and helped writing the report; RH and AG performed and analyzed the WES studies, AN analyzed and interpreted the WES studies and helped writing the report; OB performed the molecular dynamics studies and helped writing the report; EHM and RGJ performed, analyzed and interpreted metabolic tracing studies and helped writing the report; BB, BM, BMD, DH, GH, JG, JLöl, JLöt, RA, RS, SD and US planned, performed and interpreted various experiments. ME, SMC and DS assessed mitochondrial super-complex formation. MG and RI performed bioinformatics analyses. AS planned, performed and analyzed proteomic experiments and helped writing the report. IH helped identifying PAD patients and performed immunologic analyses. CRK, ME, NC and RB helped with recruiting PAD patients and coordinated clinical characterization and analyses. MR organized and supervised the PAD patient cohort, contributed to conceiving the study, supervised and advised experiments, analyzed and interpreted data, and helped writing the report. CH conceived the study, supervised and coordinated the research and wrote the report.

DATA AVAILABILITY STATEMENT

Web links for publicly available datasets are provided at the appropriate places in the manuscript, accession codes for RNAseq and WES data will be made available upon publication. No restrictions on data availability apply. All figure panels, with exception of Figure S5g, are associated with raw data.

REFERENCES

1. Picard, C. *et al.* International Union of Immunological Societies: 2017 Primary Immunodeficiency Diseases Committee Report on Inborn Errors of Immunity. *Journal of Clinical Immunology* **38,** 96–128 (2018).
2. Fried, A. J. & Bonilla, F. A. Pathogenesis, diagnosis, and management of primary antibody deficiencies and infections. *Clin. Microbiol. Rev.* **22,** 396–414 (2009).
3. Durandy, A., Kracker, S. & Fischer, A. Primary antibody deficiencies. *Nat. Rev. Immunol.* **13,** 519–533 (2013).
4. Minegishi, Y. *et al.* An essential role for BLNK in human B cell development. *Science* **286,** 1954–1957 (1999).
5. van Zelm PhD, M. C. *et al.* Human CD19 and CD40L deficiencies impair antibody selection and differentially affect somatic hypermutation. *J. Allergy Clin. Immunol.* **134,** 135–144.e7 (2014).
6. Silva, P. *et al.* Autosomal recessive agammaglobulinemia due to defect in μ heavy chain caused by a novel mutation in the IGHM gene. *Nature Publishing Group* **18,** 197–199 (2017).
7. Fischer, A. *et al.* Autoimmune and inflammatory manifestations occur frequently in patients with primary immunodeficiencies. *J. Allergy Clin. Immunol.* **140,** 1388–1393.e8 (2017).
8. Dimeloe, S., Burgener, A.-V., Grählert, J. & Hess, C. T-cell metabolism governing activation, proliferation and differentiation; a modular view. *Immunology* (2016). doi:10.1111/imm.12655
9. Hess, C. & Kemper, C. Complement-Mediated Regulation of Metabolism and Basic Cellular Processes. *Immunity* **45,** 240–254 (2016).
10. Bantug, G. R., Galluzzi, L., Kroemer, G. & Hess, C. The spectrum of T cell metabolism in health and disease. *Nat. Rev. Immunol.* **18,** 19–34 (2018).
11. Pearce, E. J. & Pearce, E. L. Immunometabolism in 2017: Driving immunity: all roads lead to metabolism. *Nat. Rev. Immunol.* **18,** 81–82 (2018).
12. Lunt, S. Y. & Vander Heiden, M. G. Aerobic glycolysis: meeting the metabolic requirements of cell proliferation. *Annu. Rev. Cell Dev. Biol.* **27,** 441–464 (2011).
13. Jellusova, J. *et al.* Gsk3 is a metabolic checkpoint regulator in B cells. *Nat. Immunol.* **18,** 303–312 (2017).
14. Boothby, M. & Rickert, R. C. Metabolic Regulation of the Immune Humoral Response. *Immunity* **46,** 743–755 (2017).
15. Carr, E. L. *et al.* Glutamine uptake and metabolism are coordinately regulated by ERK/MAPK during T lymphocyte activation. *J. Immunol.* **185,** 1037–1044 (2010).
16. Wang, R. *et al.* The transcription factor Myc controls metabolic reprogramming upon T lymphocyte activation. *Immunity* **35,** 871–882 (2011).
17. Jiang, S., Yan, W., Wang, S. E. & Baltimore, D. Let-7 Suppresses B Cell Activation through Restricting the Availability of Necessary Nutrients. *Cell Metab.* **27,** 393–403.e4 (2018).
18. Mehta, M. M., Weinberg, S. E. & Chandel, N. S. Mitochondrial control of immunity: beyond ATP. *Nat. Rev. Immunol.* **17,** 608–620 (2017).
19. Ernster, L. Mitochondria: a historical review. *The Journal of Cell Biology* **91,** 227s–255 (1981).
20. Martínez-Reyes, I. *et al.* TCA Cycle and Mitochondrial Membrane Potential Are Necessary for Diverse Biological Functions. *Mol. Cell* **61,** 199–209 (2016).
21. van der Windt, G. J. W. *et al.* Mitochondrial respiratory capacity is a critical regulator of CD8+ T cell memory development. *Immunity* **36,** 68–78 (2012).
22. Schurich, A. *et al.* Distinct Metabolic Requirements of Exhausted and Functional Virus-Specific CD8 T Cells in the Same Host. *Cell Rep* **16,** 1243–1252 (2016).
23. Tan, H. *et al.* Integrative Proteomics and Phosphoproteomics Profiling Reveals Dynamic Signaling Networks and Bioenergetics Pathways Underlying T Cell Activation. *Immunity* **46,** 488–503 (2017).

24. Tannahill, G. M. *et al.* Succinate is an inflammatory signal that induces IL-1β through HIF-1α. *Nature* **496,** 238–242 (2013).
25. Sena, L. A. *et al.* Mitochondria are required for antigen-specific T cell activation through reactive oxygen species signaling. *Immunity* **38,** 225–236 (2013).
26. Ogura, M. *et al.* Mitochondrial reactive oxygen species suppress humoral immune response through reduction of CD19 expression in B cells in mice. *Eur. J. Immunol.* **47,** 406–418 (2017).
27. Gubser, P. M. *et al.* Rapid effector function of memory CD8+ T cells requires an immediate-early glycolytic switch. *Nat. Immunol.* **14,** 1064–1072 (2013).
28. Bantug, G. R. *et al.* Mitochondria-Endoplasmic Reticulum Contact Sites Function as Immunometabolic Hubs that Orchestrate the Rapid Recall Response of Memory CD8+T Cells. *Immunity* (2018). doi:10.1016/j.immuni.2018.02.012
29. Xiao, M. *et al.* Inhibition of α-KG-dependent histone and DNA demethylases by fumarate and succinate that are accumulated in mutations of FH and SDH tumor suppressors. *Genes Dev.* **26,** 1326–1338 (2012).
30. Laukka, T. *et al.* Fumarate and Succinate Regulate Expression of Hypoxia-inducible Genes via TET Enzymes. *J. Biol. Chem.* **291,** 4256–4265 (2016).
31. Arts, R. J. W. *et al.* Glutaminolysis and Fumarate Accumulation Integrate Immunometabolic and Epigenetic Programs in Trained Immunity. *Cell Metab.* **24,** 807–819 (2016).
32. Liu, P.-S. *et al.* α-ketoglutarate orchestrates macrophage activation through metabolic and epigenetic reprogramming. *Nat. Immunol.* **18,** 985–994 (2017).
33. Alderson, N. L. *et al.* S-(2-Succinyl)cysteine: a novel chemical modification of tissue proteins by a Krebs cycle intermediate. *Arch. Biochem. Biophys.* **450,** 1–8 (2006).
34. Ternette, N. *et al.* Inhibition of mitochondrial aconitase by succination in fumarate hydratase deficiency. *Cell Rep* **3,** 689–700 (2013).
35. Kornberg, M. D. *et al.* Dimethyl fumarate targets GAPDH and aerobic glycolysis to modulate immunity. *Science* **17,** eaan4665 (2018).
36. Blatnik, M., Thorpe, S. R. & Baynes, J. W. Succination of proteins by fumarate: mechanism of inactivation of glyceraldehyde-3-phosphate dehydrogenase in diabetes. *Ann. N. Y. Acad. Sci.* **1126,** 272–275 (2008).
37. Adam, J. *et al.* Renal cyst formation in Fh1-deficient mice is independent of the Hif/Phd pathway: roles for fumarate in KEAP1 succination and Nrf2 signaling. *Cancer Cell* **20,** 524–537 (2011).
38. Gordon, D. S., Jones, B. M., Browning, S. W., Spira, T. J. & Lawrence, D. N. Persistent polyclonal lymphocytosis of B lymphocytes. *N. Engl. J. Med.* **307,** 232–236 (1982).
39. Troussard, X. *et al.* Persistent polyclonal lymphocytosis with binucleated B lymphocytes: a genetic predisposition. *Br. J. Haematol.* **88,** 275–280 (1994).
40. Carr, R., Fishlock, K. & Matutes, E. Persistent polyclonal B-cell lymphocytosis in identical twins. *Br. J. Haematol.* **96,** 272–274 (1997).
41. Cornet, E. *et al.* Long-term follow-up of 111 patients with persistent polyclonal B-cell lymphocytosis with binucleated lymphocytes. *Leukemia* **23,** 419–422 (2009).
42. Bhagwandin, S. B., Weisenberg, E. S., Ozer, H. & Maker, A. V. Symptomatic Massive Splenomegaly in Persistent Polyclonal B-cell Lymphocytosis Requiring Splenectomy. *Open J Clin Med Case Rep* **1,** (2015).
43. Salabei, J. K., Gibb, A. A. & Hill, B. G. Comprehensive measurement of respiratory activity in permeabilized cells using extracellular flux analysis. *Nat Protoc* **9,** 421–438 (2014).
44. Huang, G. *et al.* GRIM-19, a cell death regulatory protein, is essential for assembly and function of mitochondrial complex I. *Mol. Cell. Biol.* **24,** 8447–8456 (2004).
45. Iverson, T. M., Maklashina, E. & Cecchini, G. Structural basis for malfunction in complex II. *J. Biol. Chem.* **287,** 35430–35438 (2012).
46. Teipel, J. W., Hass, G. M. & Hill, R. L. The substrate specificity of fumarase. *J. Biol. Chem.* **243,** 5684–5694 (1968).

47. Cerutti, A., Cols, M. & Puga, I. Marginal zone B cells: virtues of innate-like antibody-producing lymphocytes. *Nat. Rev. Immunol.* **13,** 118–132 (2013).
48. Seifert, M. *et al.* Functional capacities of human IgM memory B cells in early inflammatory responses and secondary germinal center reactions. *Proc. Natl. Acad. Sci. U.S.A.* **112,** E546–55 (2015).
49. Sims-Mourtada, J. C. *et al.* In vivo expression of interleukin-8, and regulated on activation, normal, T-cell expressed, and secreted, by human germinal centre B lymphocytes. *Immunology* **110,** 296–303 (2003).
50. Dinarello, C. A. Immunological and inflammatory functions of the interleukin-1 family. *Annu. Rev. Immunol.* **27,** 519–550 (2009).
51. Zhang, D., Sun, M., Samols, D. & Kushner, I. STAT3 participates in transcriptional activation of the C-reactive protein gene by interleukin-6. *J. Biol. Chem.* **271,** 9503–9509 (1996).
52. Slaats, J., Oever, Ten, J., van de Veerdonk, F. L. & Netea, M. G. IL-1β/IL-6/CRP and IL-18/ferritin: Distinct Inflammatory Programs in Infections. *PLoS Pathog.* **12,** e1005973 (2016).
53. Barshir, R., Shwartz, O., Smoly, I. Y. & Yeger-Lotem, E. Comparative analysis of human tissue interactomes reveals factors leading to tissue-specific manifestation of hereditary diseases. *PLoS Comput Biol* **10,** e1003632 (2014).
54. Schaefer, M. H. & Serrano, L. Cell type-specific properties and environment shape tissue specificity of cancer genes. *Sci Rep* **6,** 20707 (2016).
55. Schwall, C. T., Greenwood, V. L. & Alder, N. N. The stability and activity of respiratory Complex II is cardiolipin-dependent. *Biochim. Biophys. Acta* **1817,** 1588–1596 (2012).
56. Hwang, M.-S., Rohlena, J., Dong, L.-F., Neuzil, J. & Grimm, S. Powerhouse down: Complex II dissociation in the respiratory chain. *Mitochondrion* **19 Pt A,** 20–28 (2014).
57. Maklashina, E., Rajagukguk, S., Iverson, T. M. & Cecchini, G. The unassembled flavoprotein subunits of human and bacterial complex II have impaired catalytic activity and generate only minor amounts of ROS. *J. Biol. Chem.* jbc.RA118.001977 (2018). doi:10.1074/jbc.RA118.001977
58. Blewett, M. M. *et al.* Chemical proteomic map of dimethyl fumarate-sensitive cysteines in primary human T cells. *Sci Signal* **9,** rs10–rs10 (2016).
59. Ruecker, N. *et al.* Fumarase Deficiency Causes Protein and Metabolite Succination and Intoxicates Mycobacterium tuberculosis. *Cell Chem Biol* **24,** 306–315 (2017).
60. Itoh, K. *et al.* Keap1 represses nuclear activation of antioxidant responsive elements by Nrf2 through binding to the amino-terminal Neh2 domain. *Genes Dev.* **13,** 76–86 (1999).
61. Kobayashi, A. *et al.* Oxidative and Electrophilic Stresses Activate Nrf2 through Inhibition of Ubiquitination Activity of Keap1. *Mol. Cell. Biol.* **26,** 221–229 (2005).
62. Kinch, L., Grishin, N. V. & Brugarolas, J. Succination of Keap1 and activation of Nrf2-dependent antioxidant pathways in FH-deficient papillary renal cell carcinoma type 2. *Cancer Cell* **20,** 418–420 (2011).
63. Taguchi, K. *et al.* Keap1 degradation by autophagy for the maintenance of redox homeostasis. *Proc. Natl. Acad. Sci. U.S.A.* **109,** 13561–13566 (2012).
64. Bollong, M. J. *et al.* A Small Molecule Inhibits Deregulated NRF2 Transcriptional Activity in Cancer. *ACS Chem. Biol.* **10,** 2193–2198 (2015).
65. Singh, A. *et al.* Small Molecule Inhibitor of NRF2 Selectively Intervenes Therapeutic Resistance in KEAP1-Deficient NSCLC Tumors. *ACS Chem. Biol.* **11,** 3214–3225 (2016).
66. Zhu, J. *et al.* An overview of chemical inhibitors of the Nrf2-ARE signaling pathway and their potential applications in cancer therapy. *Free Radic. Biol. Med.* **99,** 544–556 (2016).
67. Yin, S. & Cao, W. Toll-Like Receptor Signaling Induces Nrf2 Pathway Activation through p62-Triggered Keap1 Degradation. *Mol. Cell. Biol.* **35,** 2673–2683 (2015).
68. Alcalá, M. *et al.* Increased inflammation, oxidative stress and mitochondrial respiration in brown adipose tissue from obese mice. *Sci Rep* **7,** 2169 (2017).
69. Wagner, G. R. & Payne, R. M. Mitochondrial Acetylation and Diseases of Aging. *Journal of Aging*

Research **2011,** 1–13 (2011).
70. Roy, J., Ryckman, C., Bernier, V., Whittom, R. & Delage, R. Large cell lymphoma complicating persistent polyclonal B cell lymphocytosis. *Leukemia* **12,** 1026–1030 (1998).
71. Tohyama, N. Growth autonomy and tumorigenicity of interleukin 6-dependent B cells transfected with interleukin 6 cDNA. *J. Exp. Med.* **171,** 389–400 (1990).
72. Jego, G. Interleukin-6 is a growth factor for nonmalignant human plasmablasts. *Blood* **97,** 1817–1822 (2001).
73. Mine, S. *et al.* Interleukin-6-dependent growth in a newly established plasmablastic lymphoma cell line and its therapeutic targets. *Sci Rep* **7,** 2323 (2017).
74. Burnichon, N. *et al.* SDHA is a tumor suppressor gene causing paraganglioma. *Human Molecular Genetics* **19,** 3011–3020 (2010).
75. Su, C.-Y., Chang, Y.-C., Yang, C.-J., Huang, M.-S. & Hsiao, M. The opposite prognostic effect of NDUFS1 and NDUFS8 in lung cancer reflects the oncojanus role of mitochondrial complex I. *Sci Rep* **6,** 85 (2016).
76. Kim, H.-C., Chang, J., Lee, H. S. & Kwon, H. J. Mitochondrial UQCRB as a new molecular prognostic biomarker of human colorectal cancer. *Exp. Mol. Med.* **49,** e391 (2017).
77. Guo, L. *et al.* Inhibition of Mitochondrial Complex II by the Anticancer Agent Lonidamine. *J. Biol. Chem.* **291,** 42–57 (2016).
78. Nath, K. *et al.* Mechanism of antineoplastic activity of lonidamine. *Biochim. Biophys. Acta* **1866,** 151–162 (2016).
79. Mills, E. L. *et al.* Itaconate is an anti-inflammatory metabolite that activates Nrf2 via alkylation of KEAP1. *Nature* (2018). doi:10.1038/nature25986
80. Lundy, S. K. *et al.* Dimethyl fumarate treatment of relapsing-remitting multiple sclerosis influences B-cell subsets. *Neurol Neuroimmunol Neuroinflamm* **3,** e211 (2016).
81. Kolbach, D. N. & Nieboer, C. Fumaric acid therapy in psoriasis: results and side effects of 2 years of treatment. *J. Am. Acad. Dermatol.* **27,** 769–771 (1992).
82. Altmeyer, P. J. *et al.* Antipsoriatic effect of fumaric acid derivatives. Results of a multicenter double-blind study in 100 patients. *J. Am. Acad. Dermatol.* **30,** 977–981 (1994).
83. Weller, S. *et al.* Human blood IgM 'memory' B cells are circulating splenic marginal zone B cells harboring a prediversified immunoglobulin repertoire. *Blood* **104,** 3647–3654 (2004).
84. Solanki, H. S. *et al.* Cigarette smoke induces metabolic reprogramming in lung cells. *3* **1,** 281–281 (2017).
85. Chen, Q. *et al.* Serum Metabolite Biomarkers Discriminate Healthy Smokers from COPD Smokers. *PLoS ONE* **10,** e0143937 (2015).
86. Speyer, C. B. & Costenbader, K. H. Cigarette smoking and the pathogenesis of systemic lupus erythematosus. *Expert Rev Clin Immunol* **14,** 481–487 (2018).
87. Bonarius, H. P. J. *et al.* Antinuclear autoantibodies are more prevalent in COPD in association with low body mass index but not with smoking history. *Thorax* **66,** 101–107 (2011).
88. Dasanu, C. A. & Codreanu, I. Persistent polyclonal B-cell lymphocytosis in chronic smokers: more than meets the eye. *Conn Med* **76,** 69–72 (2012).
89. Brandsma, C.-A. *et al.* Increased levels of (class switched) memory B cells in peripheral blood of current smokers. *Respir. Res.* **10,** 108 (2009).
90. Longbrake, E. E. *et al.* Dimethyl fumarate induces changes in B- and T-lymphocyte function independent of the effects on absolute lymphocyte count. *Mult. Scler.* **24,** 728–738 (2018).
91. Honda, S.-I. *et al.* Marginal zone B cells exacerbate endotoxic shock via interleukin-6 secretion induced by Fcα/μR-coupled TLR4 signalling. *Nature Communications* **7,** 11498 (2016).
92. Daridon, C. *et al.* Identification of transitional type II B cells in the salivary glands of patients with Sjögren's syndrome. *Arthritis Rheum.* **54,** 2280–2288 (2006).
93. Shen, L. *et al.* Central role for marginal zone B cells in an animal model of Sjogren's syndrome. *Clin. Immunol.* **168,** 30–36 (2016).
94. Plotkin, J. B. & Kudla, G. Synonymous but not the same: the causes and consequences of codon

bias. *Nat. Rev. Genet.* **12,** 32–42 (2011).
95. Chaney, J. L. & Clark, P. L. Roles for Synonymous Codon Usage in Protein Biogenesis. *Annu Rev Biophys* **44,** 143–166 (2015).
96. Thorvaldsdóttir, H., Robinson, J. T. & Mesirov, J. P. Integrative Genomics Viewer (IGV): high-performance genomics data visualization and exploration. *Brief. Bioinformatics* **14,** 178–192 (2013).
97. Hunt, R. C., Simhadri, V. L., Iandoli, M., Sauna, Z. E. & Kimchi-Sarfaty, C. Exposing synonymous mutations. *Trends Genet.* **30,** 308–321 (2014).
98. Wittig, I., Braun, H.-P. & Schägger, H. Blue native PAGE. *Nat Protoc* **1,** 418–428 (2006).
99. Faubert, B. *et al.* Loss of the tumor suppressor LKB1 promotes metabolic reprogramming of cancer cells via HIF-1α. *Proc. Natl. Acad. Sci. U.S.A.* **111,** 2554–2559 (2014).
100. McGuirk, S. *et al.* PGC-1α supports glutamine metabolism in breast cancer. *Cancer Metab* **1,** 22 (2013).
101. McKenna, A. *et al.* The Genome Analysis Toolkit: a MapReduce framework for analyzing next-generation DNA sequencing data. *Genome Research* **20,** 1297–1303 (2010).
102. Kircher, M. *et al.* A general framework for estimating the relative pathogenicity of human genetic variants. *Nat. Genet.* **46,** 310–315 (2014).
103. McLaren, W. *et al.* The Ensembl Variant Effect Predictor. *Genome Biol.* **17,** 122 (2016).
104. Robinson, J. T. *et al.* Integrative genomics viewer. *Nat. Biotechnol.* **29,** 24–26 (2011).
105. Reese, M. G., Eeckman, F. H., Kulp, D. & Haussler, D. Improved splice site detection in Genie. *J. Comput. Biol.* **4,** 311–323 (1997).
106. Agarwal, V., Bell, G. W., Nam, J.-W. & Bartel, D. P. Predicting effective microRNA target sites in mammalian mRNAs. *Elife* **4,** 101 (2015).
107. Koboldt, D. C. *et al.* VarScan 2: somatic mutation and copy number alteration discovery in cancer by exome sequencing. *Genome Research* **22,** 568–576 (2012).
108. Cibulskis, K. *et al.* Sensitive detection of somatic point mutations in impure and heterogeneous cancer samples. *Nat. Biotechnol.* **31,** 213–219 (2013).
109. Saunders, C. T. *et al.* Strelka: accurate somatic small-variant calling from sequenced tumor-normal sample pairs. *Bioinformatics* **28,** 1811–1817 (2012).
110. Inaoka, D. K. *et al.* Structural Insights into the Molecular Design of Flutolanil Derivatives Targeted for Fumarate Respiration of Parasite Mitochondria. *Int J Mol Sci* **16,** 15287–15308 (2015).
111. Biasini, M. *et al.* SWISS-MODEL: modelling protein tertiary and quaternary structure using evolutionary information. *Nucleic Acids Res.* **42,** W252–8 (2014).
112. Humphrey, W., Dalke, A. & Schulten, K. VMD: visual molecular dynamics. *J Mol Graph* **14,** 33–8– 27–8 (1996).
113. Pettersen, E. F. *et al.* UCSF Chimera--a visualization system for exploratory research and analysis. *J Comput Chem* **25,** 1605–1612 (2004).
114. Huo, X. *et al.* Preliminary molecular characterization and crystallization of mitochondrial respiratory complex II from porcine heart. *FEBS J.* **274,** 1524–1529 (2007).
115. Vanommeslaeghe, K. *et al.* CHARMM general force field: A force field for drug-like molecules compatible with the CHARMM all-atom additive biological force fields. *J Comput Chem* **31,** 671–690 (2010).
116. Irwin, J. J., Sterling, T., Mysinger, M. M., Bolstad, E. S. & Coleman, R. G. ZINC: a free tool to discover chemistry for biology. *J Chem Inf Model* **52,** 1757–1768 (2012).
117. Bussi, G. Hamiltonian replica exchange in GROMACS: a flexible implementation. *Molecular Physics* **112,** 379–384 (2014).
118. Jorgensen, W. L., Chandrasekhar, J., Madura, J. D., Impey, R. W. & Klein, M. L. Comparison of simple potential functions for simulating liquid water. *The Journal of Chemical Physics* **79,** 926–935 (1983).
119. Parrinello, M. & Rahman, A. Polymorphic transitions in single crystals: A new molecular

dynamics method. *Journal of Applied Physics* **52,** 7182–7190 (1981).
120. Hoover, W. Canonical dynamics: Equilibrium phase-space distributions. *Phys Rev A Gen Phys* **31,** 1695–1697 (1985).
121. Patriksson, A. & van der Spoel, D. A temperature predictor for parallel tempering simulations. *Phys Chem Chem Phys* **10,** 2073–2077 (2008).
122. Hess, B. P-LINCS: A Parallel Linear Constraint Solver for Molecular Simulation. *J Chem Theory Comput* **4,** 116–122 (2008).
123. Zeileis, A. & Grothendieck, G. zoo: S3Infrastructure for Regular and Irregular Time Series. *Journal of Statistical Software* **14,** 1–27 (2005).